NuSTAR REVEALS EXTREME ABSORPTION IN $z < 0.5$ TYPE 2 QUASARS

G. B. Lansbury[1], P. Gandhi[1,2], D. M. Alexander[1], R. J. Assef[3], J. Aird[4], A. Annuar[1], D. R. Ballantyne[5], M. Baloković[6], F. E. Bauer[7,8,9], S. E. Boggs[10], W. N. Brandt[11,12], M. Brightman[6], F. E. Christensen[13], F. Civano[14,15,16], A. Comastri[17], W. W. Craig[13,18], A. Del Moro[1], B. W. Grefenstette[6], C. J. Hailey[19], F. A. Harrison[6], R. C. Hickox[16], M. Koss[20], S. M. LaMassa[14], B. Luo[11,12], S. Puccetti[21,22], D. Stern[23], E. Treister[24], C. Vignali[17,25], L. Zappacosta[22], AND W. W. Zhang[26]

[1] Centre for Extragalactic Astronomy, Department of Physics, University of Durham, South Road, Durham DH1 3LE, UK; g.b.lansbury@durham.ac.uk
[2] School of Physics and Astronomy, University of Southampton, Highfield, Southampton SO17 1BJ, UK
[3] Núcleo de Astronomía de la Facultad de Ingeniería, Universidad Diego Portales, Av. Ejército Libertador 441, Santiago, Chile
[4] Institute of Astronomy, University of Cambridge, Madingley Road, Cambridge, CB3 0HA, UK
[5] Center for Relativistic Astrophysics, School of Physics, Georgia Institute of Technology, Atlanta, GA 30332, USA
[6] Cahill Center for Astrophysics, 1216 East California Boulevard, California Institute of Technology, Pasadena, CA 91125, USA
[7] Instituto de Astrofísica, Facultad de Física, Pontificia Universidad Católica de Chile, 306, Santiago 22, Chile
[8] Millennium Institute of Astrophysics, Vicuña Mackenna 4860, 7820436 Macul, Santiago, Chile
[9] Space Science Institute, 4750 Walnut Street, Suite 205, Boulder, CO 80301, USA
[10] Space Sciences Laboratory, University of California, Berkeley, CA 94720, USA
[11] Department of Astronomy and Astrophysics, 525 Davey Lab, The Pennsylvania State University, University Park, PA 16802, USA
[12] Institute for Gravitation and the Cosmos, The Pennsylvania State University, University Park, PA 16802, USA
[13] DTU Space-National Space Institute, Technical University of Denmark, Elektrovej 327, DK-2800 Lyngby, Denmark
[14] Yale Center for Astronomy and Astrophysics, Physics Department, Yale University, P.O. Box 208120, New Haven, CT 06520-8120, USA
[15] Smithsonian Astrophysical Observatory, 60 Garden Street, Cambridge, MA 02138, USA
[16] Department of Physics and Astronomy, Dartmouth College, 6127 Wilder Laboratory, Hanover, NH 03755, USA
[17] INAF Osservatorio Astronomico di Bologna, via Ranzani 1, I-40127 Bologna, Italy
[18] Lawrence Livermore National Laboratory, Livermore, CA 94550, USA
[19] Columbia Astrophysics Laboratory, 550 W 120th Street, Columbia University, NY 10027, USA
[20] Institute for Astronomy, Department of Physics, ETH Zurich, Wolfgang-Pauli-Strasse 27, CH-8093 Zurich, Switzerland
[21] ASDC-ASI, Via del Politecnico, I-00133 Roma, Italy
[22] INAF Osservatorio Astronomico di Roma, via Frascati 33, I-00040 Monte Porzio Catone (RM), Italy
[23] Jet Propulsion Laboratory, California Institute of Technology, 4800 Oak Grove Drive, Mail Stop 169-221, Pasadena, CA 91109, USA
[24] Universidad de Concepción, Departamento de Astronomía, Casilla 160-C, Concepción, Chile
[25] Dipartimento di Fisica e Astronomia, Università degli Studi di Bologna, Viale Berti Pichat 6/2, I-40127 Bologna, Italy
[26] NASA Goddard Space Flight Center, Greenbelt, MD 20771, USA

ABSTRACT

The intrinsic column density ($N_{\rm H}$) distribution of quasars is poorly known. At the high obscuration end of the quasar population and for redshifts $z < 1$, the X-ray spectra can only be reliably characterized using broad-band measurements that extend to energies above 10 keV. Using the hard X-ray observatory *NuSTAR*, along with archival *Chandra* and *XMM-Newton* data, we study the broad-band X-ray spectra of nine optically selected (from the SDSS), candidate Compton-thick ($N_{\rm H} > 1.5 \times 10^{24}$ cm^{-2}) type 2 quasars (CTQSO2s); five new *NuSTAR* observations are reported herein, and four have been previously published. The candidate CTQSO2s lie at $z < 0.5$, have observed [O III] luminosities in the range $8.4 < \log(L_{\rm [O\ III]}/L_\odot) < 9.6$, and show evidence for extreme, Compton-thick absorption when indirect absorption diagnostics are considered. Among the nine candidate CTQSO2s, five are detected by *NuSTAR* in the high-energy (8–24 keV) band: two are weakly detected at the $\approx 3\sigma$ confidence level and three are strongly detected with sufficient counts for spectral modeling ($\gtrsim 90$ net source counts at 8–24 keV). For these *NuSTAR*-detected sources *direct* (i.e., X-ray spectral) constraints on the intrinsic active galactic nucleus properties are feasible, and we measure column densities ≈ 2.5–1600 times higher and intrinsic (unabsorbed) X-ray luminosities ≈ 10–70 times higher than pre-*NuSTAR* constraints from *Chandra* and *XMM-Newton*. Assuming the *NuSTAR*-detected type 2 quasars are representative of other Compton-thick candidates, we make a correction to the $N_{\rm H}$ distribution for optically selected type 2 quasars as measured by *Chandra* and *XMM-Newton* for 39 objects. With this approach, we predict a Compton-thick fraction of $f_{\rm CT} = 36^{+14}_{-12}$ %, although higher fractions (up to 76%) are possible if indirect absorption diagnostics are assumed to be reliable.

Key words: galaxies: active – X-rays: galaxies

1. INTRODUCTION

Much of the cosmic growth of supermassive black holes is thought to occur during a phase of luminous, heavily obscured accretion: an obscured quasar phase (e.g., Fabian 1999; Gilli et al. 2007; Treister et al. 2009). However, our current census of obscured quasars appears highly incomplete. While unobscured quasars were first discovered over 50 years ago

(Hazard et al. 1963; Schmidt 1963), it is only in the last decade that (radio-quiet) obscured quasars have been discovered in large numbers (e.g., Zakamska et al. 2003; Hickox et al. 2007; Reyes et al. 2008; Stern et al. 2012; Assef et al. 2013; Donoso et al. 2014). Furthermore, it is only very recently that the most heavily obscured Compton-thick (with absorbing column densities of $N_{\rm H} > 1.5 \times 10^{24}$ cm^{-2}; hereafter CT) quasars have begun to be robustly identified at X-ray energies (e.g., Comastri

et al. 2011; Gilli et al. 2011; Gandhi et al. 2014; Lanzuisi et al. 2015b).

Identifying and characterizing heavily obscured quasars is important for various reasons. First, many less luminous active galactic nuclei (AGNs) in the local universe appear to be CT ($\sim$20%–30% of the total population; e.g., Risaliti et al. 1999; Burlon et al. 2011). While observational constraints are challenging for distant quasars, a significant population of luminous CT AGNs are expected from models of the cosmic X-ray background (CXB) spectrum (e.g., Comastri et al. 1995; Gilli et al. 2007; Treister et al. 2009; Draper & Ballantyne 2010; Akylas et al. 2012; Ueda et al. 2014). Second, while the orientation-based unified model (e.g., Antonucci 1993; Urry & Padovani 1995) can account for the relative fractions of unobscured, obscured, and CT AGNs observed in the local universe, it is unclear whether a unified model or some evolutionary scenario (e.g., Sanders et al. 1988; Hopkins et al. 2008) is more appropriate at higher luminosities and redshifts. Indeed, the observed dependence of AGN obscuration on luminosity suggests a departure from the unified model (e.g., Ueda et al. 2003; Simpson 2005, Treister et al. 2010, Iwasawa et al. 2012; Assef et al. 2015, Buchner et al. 2015, Lacy et al. 2015). The above issues can be addressed using X-ray studies that aim to measure the column density (N_H) distribution and CT fraction of obscured quasars, which are important components of CXB models and important tools for understanding AGN models (e.g., Fabian et al. 2009; Draper & Ballantyne 2010).

X-ray studies of heavily obscured quasars are extremely challenging. For instance, to date very few optically selected obscured quasars (i.e., "type 2" quasars or "QSO2s"; the definition of this term is provided in Section 2.1) have been unambiguously confirmed as CT using broad-band X-ray measurements extending to high energies ($>$10 keV; e.g., Gandhi et al. 2014). Including the high-energy data is crucial. First, the number of counts is inherently low at $<$10 keV due to photoelectric absorption of the X-ray continuum, which restricts the accuracy of X-ray spectral modeling and may lead to an underestimate of the absorbing column density and intrinsic luminosity. Second, important diagnostic features can be missed if the observed X-ray energy window is narrow. Such features include the photoelectric absorption cut-off (e.g., at $\approx$10 keV for a $z = 0.2$ AGN absorbed by $N_H = 10^{24}$ cm^{-2} gas), and features of Compton reflection/scattering from cold, dense gas. The latter become prominent when CT levels of photoelectric absorption deeply suppress the primary continuum, revealing strong Fe Kα fluorescent line emission at 6.4 keV and a Compton reflection "hump" at $>$10 keV (e.g., George & Fabian 1991), and they may arise from an extended structure such as the torus of the unified model (e.g., Ghisellini et al. 1994).

NuSTAR (Harrison et al. 2013), launched in 2012 June, has further opened our window on the X-ray spectra of obscured AGNs, with sensitivity up to 78.4 keV. As the first orbiting observatory to focus high-energy ($>$10 keV) X-rays, it provides a two order of magnitude improvement in sensitivity and over an order of magnitude improvement in angular resolution relative to the previous generation $>$10 keV observatories. Recent studies have demonstrated that, in the case of heavily obscured quasars, the most accurate constraints on the absorbing column density and intrinsic X-ray luminosity come from a combination of both *NuSTAR* and *XMM-Newton/Chandra* data, which provide the broadest possible energy band pass for X-ray spectral modeling (e.g., Luo et al. 2013; Baloković et al. 2014; Del Moro et al. 2014; Gandhi et al. 2014; Lansbury et al. 2014).

In this paper, we extend the work of Lansbury et al. (2014; hereafter L14) and Gandhi et al. (2014; hereafter G14), using *NuSTAR* to study the high-energy emission of SDSS-selected QSO2s which are candidates for being CT (i.e., candidate "CTQSO2s"). The targets were initially selected based on [O III] λ5007 line emission (Zakamska et al. 2003; Reyes et al. 2008), which is thought to be an unbiased indicator of intrinsic AGN power (e.g., Heckman et al. 2005; LaMassa et al. 2010; but see also Hainline et al. 2013), and subsequently identified as CT candidates within the detection capabilities of *NuSTAR* using the low-energy X-ray data available (e.g., Jia et al. 2013). L14 looked at an exploratory sample of three $z = 0.41$–0.49 candidate CTQSO2s: one was weakly detected and shown to have a high column density of $N_H \gtrsim 5 \times 10^{23}$ cm^{-2}; the remaining two were undetected but shown to have suppressed X-ray luminosities in the high-energy regime, suggestive of CT absorption. G14 showed the lower redshift object SDSS J1034+6001 (also known as Mrk 34; $z = 0.05$) to have a column density and intrinsic power an order of magnitude greater than those measured with the pre-*NuSTAR* X-ray data, unambiguously revealing the object to be a CTQSO2.

We present new results for a further five targets, bringing the *NuSTAR*-observed SDSS-selected candidate CTQSO2 sample to a total size of nine objects. For the brightest two sources we model the broad-band X-ray spectra, for one weakly detected source we characterize the spectrum using the X-ray band ratio, and for all targets (including non-detections) we use the X-ray: mid-IR ratio to infer the intrinsic AGN properties. The paper is organized as follows: Section 2 details the sample selection; Section 3 describes the X-ray and multiwavelength data, along with data reduction and analysis procedures; Section 4 presents the results of X-ray spectral and multiwavelength analyses; and Section 5 discusses the results for the full sample of nine *NuSTAR*-observed candidate CTQSO2s in the context of the parent QSO2 population, including an estimation of the N_H distribution and CT fraction for $z < 0.5$. The cosmology adopted is $(\Omega_M, \Omega_\Lambda, h) = (0.27, 0.73, 0.71)$. Uncertainties and limits quoted throughout the paper correspond to the 90% confidence levels (CLs), unless otherwise stated.

2. THE QSO2 SAMPLE

2.1. Definitions

Quasars are rapidly accreting black holes that emit large amounts of radiation and have luminosities that typically place them above the knee of the AGN luminosity function. Multiple thresholds exist in the literature for separating quasars from less luminous AGNs (e.g., "Seyferts"). According to the classical threshold of Schmidt & Green (1983), quasars are those objects with absolute B-band magnitudes of $M_B < -23$. Thus far we have used the term "obscured" rather loosely since it has different implications depending on the wavelength regime in question. In the optical band, objects are identified as obscured if they show narrow line emission without broad (e.g., Hα or Hβ) components, a result of the central broad line region being hidden from the observer. These objects are classed as type 2s, or QSO2s if the luminosity is at quasar levels (in type 1s the broad line components are visible). At X-ray energies, objects

are identified as obscured or "absorbed" if their X-ray continua show evidence for being absorbed by gas along the line of sight, with column densities of $N_H > 10^{22} \, cm^{-2}$. The objects in this work originate from a sample of optically identified QSO2s (Zakamska et al. 2003; Reyes et al. 2008). Several X-ray studies at <10 keV have now provided evidence that these optically identified QSO2s are also absorbed at X-ray energies, with many objects showing indirect evidence for being absorbed by column densities in excess of $N_H = 1.5 \times 10^{24} \, cm^{-2}$ (i.e., CT columns; Vignali et al. 2006, 2010; Jia et al. 2013). In this paper we look at the *direct* evidence for CT absorption in these optically identified QSO2s from X-ray analyses that incorporate spectral information at >10 keV.

2.2. Sample Selection

When selecting a sample of obscured quasars to observe at X-ray energies, it is important to select based on an indicator of the intrinsic AGN luminosity such that the sample is unbiased and as representative of the general population as possible. The [O III]$\lambda 5007$ line, one of the strongest emission lines readily visible in the optical, is a suitable choice since such emission arises from gas on large (~ 100 pc) scales, minimizing the effect of nuclear obscuration. Reyes et al. (2008, hereafter R08; see also Zakamska et al. 2003) presented the largest sample of [O III]-selected QSO2s, consisting of 887 objects selected from the SDSS. R08 defined quasars as having observed (i.e., not corrected for extinction) [O III] luminosities of $L_{[O III]} > 2 \times 10^8 L_\odot$, and identified the quasars as type 2s (i.e., QSO2s) following the standard optical definition. For comparison, the classical absolute magnitude cut of Schmidt & Green (1983, $M_B < -23$) corresponds approximately to $L_{[O III]} > 3 \times 10^8 L_\odot$ for type 1 sources (Zakamska et al. 2003). Subsequent *Chandra* and *XMM-Newton* studies (e.g., Ptak et al. 2006; Vignali et al. 2006, 2010; Jia et al. 2013; LaMassa et al. 2014) have investigated the soft X-ray (<10 keV) properties of subsamples of the R08 sample, with the largest subsample (71 objects) investigated by Jia et al. (2013, hereafter J13). Figure 1 shows redshift versus $L_{[O III]}$ for the R08 and J13 samples.

For our study, we select from the J13 sample. In order to infer information about the overall optically selected QSO2 population, we desire a parameter space for which the J13 sample is broadly representative of the R08 sample. As such we apply redshift and luminosity cuts of $z < 0.5$ and $L_{[O III]} > 2.5 \times 10^8 L_\odot$, respectively (see Figure 1). For these z and $L_{[O III]}$ ranges: (1) the z and $L_{[O III]}$ distributions of the J13 sample and the R08 sample are consistent according to the Kolmogorov–Smirnov (KS) test ($p = 0.64$ and 0.09 for z and $L_{[O III]}$, respectively) and (2) the majority (74%) of the J13 sample are either serendipitous sources in the soft X-ray (*Chandra* and *XMM-Newton*) data or were targeted based on their [O III] properties, and should therefore be relatively unbiased with respect to the X-ray properties of the R08 sample. We exclude SDSS J0913+4056 ($z = 0.442$; $L_{[O III]} = 2.1 \times 10^{10} L_\odot$) since this infrared bright AGN is an extreme outlier and has been targeted for *NuSTAR* separately (D. Farrah et al. 2015, in preparation). The above cuts leave 42 QSO2s from J13, 39 of which are detected at <10 keV (according to J13 and Vignali et al. 2006, 2010).

From the J13 subsample above, we first targeted an initial three candidate CTQSO2s at $z \approx 0.4$–0.5 (this subselection is
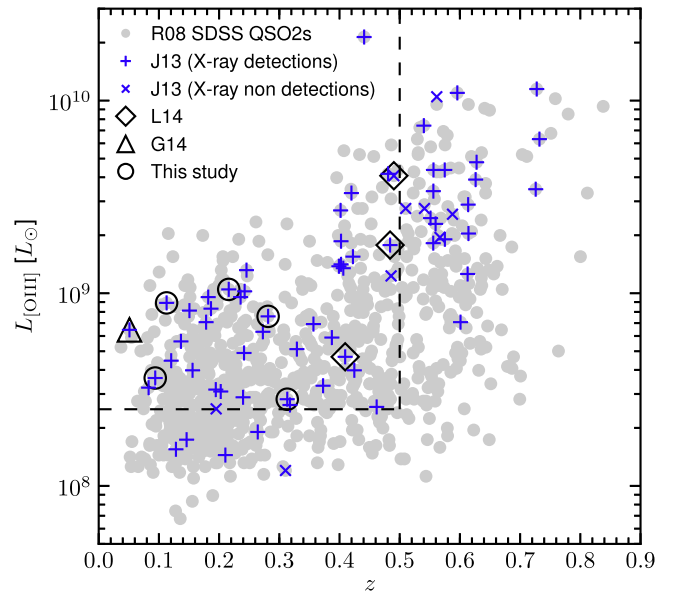

Figure 1. Observed (i.e., extinction-uncorrected) [O III] $\lambda 5007$ line luminosity ($L_{[O III]}$) vs. redshift (z). The R08 sample of SDSS-QSO2s is shown as gray dots. The J13 sample of *Chandra*- and *XMM-Newton*-observed objects is indicated in blue, with "+" and "×" symbols indicating <10 keV detections and non-detections, respectively (according to X-ray analyses in J13 and Vignali et al. 2006, 2010). The dashed lines mark the parameter space used in this work ($z < 0.5$ and $L_{[O III]} > 2.5 \times 10^8 L_\odot$), for which the J13 sample is broadly representative of the R08 sample. Our *NuSTAR*-observed subsample of candidate CTQSO2s is highlighted by black points, with circles marking the five recently observed objects presented in this study, diamonds marking the three $z \approx 0.4$–0.5 objects presented in L14, and the triangle marking the low redshift ($z = 0.05$) object presented in G14.

described in L14). Since these three objects were weakly or not detected with *NuSTAR*, for the succeeding targets described herein greater consideration was given to the predicted *NuSTAR* 8–24 keV count rate.[27] The predictions were achieved by extrapolating from the <10 keV data, assuming a variety of physically motivated torus models which cover a range of column densities ($10^{23} < N_H < 10^{25} \, cm^{-2}$). To the remainder of the J13 subsample above, we applied a cut in the observed X-ray:[O III] luminosity ratio of $L_{2-10 \, keV}^{obs}/L_{[O III]} < 1$ (a conservative threshold for targeting the most obscured candidates; see Section 4.5 in J13), which leaves 12 CT candidates. From this selection, six objects were observed with *NuSTAR*, with preference being given to the objects with high 8–24 keV count rate predictions. These include the one object presented in G14 and the five presented in this paper, bringing the *NuSTAR*-observed SDSS-selected candidate CTQSO2 sample to a total size of nine objects.

In this work we present results for the five recently observed candidate CTQSO2s SDSS J0758+3923, 0840+3838, 1218 +4706, 1243–0232, and 1713+5729. For the other four previously studied objects (SDSS J0011+0056, 0056+0032, 1034+6001, and 1157+6003) the detailed reductions and data analyses are presented in L14 and G14. Redshifts and [O III] luminosities for the five new objects are listed in Table 1. The low-energy (<10 keV) X-ray spectra have previously been characterized by J13, who fit the existing *Chandra* and *XMM-Newton* data with absorbed power law models. For SDSS J1218+4706, the column density constrained by J13 using this

---

[27] The 8–24 keV band is the standard hard band defined for the *NuSTAR* extragalactic surveys (Alexander et al. 2013).

Table 1
X-Ray Observation Log

Object Name (1)	z (2)	$L_{[O\,III]}$ (3)	*NuSTAR* Observations				Soft X-Ray Observations			
			Observation ID (4)	UT Date (5)	t_{on} (6)	t_{eff} (7)	Observatory (8)	Observation ID (9)	UT Date (10)	t (11)
SDSS J075820.98+392336.0	0.216	9.02	60001131002	2014:255	48.3	41.2	*XMM-Newton*	0305990101	2006:108	9.1
								0406740101	2006:295	14.2
SDSS J084041.08+383819.8	0.313	8.45	60001132002	2014:121	50.5	38.4	*XMM-Newton*	0502060201	2007:289	19.0
SDSS J121839.40+470627.7	0.094	8.56	60001135002	2014:145	41.8	34.0	*XMM-Newton*	0203270201	2004:153	40.8
								0400560301	2006:321	43.2
SDSS J124337.34−023200.2	0.281	8.88	60001136002	2014:211	55.5	46.0	*Chandra*	6805	2006:115	10.0
SDSS J171350.32+572954.9	0.113	8.95	60001137002	2014:120	54.5	45.3	*XMM-Newton*	0305750401	2005:174	4.4

Notes. (1) Full SDSS object name. (2) Redshift. (3) Gaussian fit [O III] $\lambda 5007$ line luminosity [$\log(L_{[O\,III]}/L_\odot)$], as reported in R08. (4) and (5) *NuSTAR* observation ID and start date (YYYY:DDD), respectively. (6) Total on-source time (ks). (7) Effective on-axis exposure time (ks). This is the net value for the 3–24 keV band and at the celestial coordinates of the target after data cleaning. We have accounted for vignetting; despite the sources being "on-axis," there is a small loss of exposure due to the natural dither of the observatory. (8), (9), and (10) Soft X-ray observatory with available data, corresponding observation ID(s), and start date(s) (YYYY:DDD), respectively. (11) Net on-axis, flaring-corrected exposure time(s) (ks). For *XMM-Newton*, the quoted value corresponds to the EPIC detector used with the longest net exposure time.

direct (i.e., X-ray spectral) approach is high, but less than CT ($N_H = 8.0^{+5.6}_{-4.1} \times 10^{23}\,cm^{-2}$). In the other four cases, the directly constrained column densities are comparatively low ($N_H < 3 \times 10^{22}\,cm^{-2}$). This is in strong disagreement with the extremely low X-ray:[O III] ratios, which imply CT absorption. J13 recognized this, and thus used indirect diagnostics to estimate the absorption levels. The low N_H measurements from direct spectral fitting can be explained as due to a combination of the limited energy ranges of *Chandra* and *XMM-Newton*, low source counts, and (especially in the case of SDSS J1713 +5729; see Section 4.1.3 for further details) strong contamination at lower energies from other processes such as star formation, AGN photoionization, or scattered AGN emission. In the Appendix we give individual object information for the five candidate CTQSO2s presented in this paper, including relevant multiwavelength properties and indicators of heavy absorption. In addition, we comment on the single *NuSTAR*-detected candidate CTQSO2 from the exploratory study of L14 (SDSS J0011+0056), for which a close inspection of the soft X-ray data reveals strong Fe Kα emission.

3. DATA

This section details the pointed *NuSTAR* observations and data analysis procedures for the five newly observed SDSS-selected candidate CTQSO2s (Section 3.1), which bring the *NuSTAR*-observed sample to a total of nine such objects. We also detail the archival *Chandra* and *XMM-Newton* data (Section 3.2), which facilitate a broad-band X-ray analysis when combined with the *NuSTAR* data. In addition, near-UV to mid-IR data from large-area surveys are presented in order to characterize the spectral energy distributions (SEDs) of the objects and disentangle AGN and host galaxy emission in the mid-IR (Section 3.3).

3.1. NuSTAR Data

The *NuSTAR* observatory is sensitive at 3–78.4 keV (Harrison et al. 2013). The combination of the instrumental background and decrease in effective area with increasing energy means that 3 to ≈ 24 keV is the most useful energy band for faint sources. *NuSTAR* consists of two telescopes (A and B), identical in design, the respective focal plane modules of which are referred to as FPMA and FPMB. The point-spread

function (PSF) has a tight "core" of FWHM $= 18''$ and a half-power diameter of $58''$.

Table 1 provides details, including dates and exposure times, for the most recent five *NuSTAR* observations of SDSS-selected candidate CTQSO2s. The data were processed as for the L14 sample, using the *NuSTAR* Data Analysis Software (NuSTAR-DAS) version 1.3.0. For the detected sources, the NUPRODUCTS task was used to extract spectra and response files. Following other recent *NuSTAR* studies (Alexander et al. 2013; L14; Luo et al. 2014), we perform photometry in the 3–24, 3–8, and 8–24 keV bands. The photometry is performed for each FPM separately and also for combined FPMA+FPMB data (referred to hereafter as "FPMA+B") to increase sensitivity. For source detection, we use prior knowledge of the SDSS coordinates and calculate no-source probabilities assuming binomial statistics (P_B), defining non-detections as $P_B > 1\%$ (i.e., $\lesssim 2.6\sigma$). For non-detections we calculate upper limits on the net source counts using the Bayesian approach outlined in Kraft et al. (1991). For a detailed description of the source detection and aperture photometry procedures, we refer the reader to L14.

Table 2 summarizes the *NuSTAR* photometry. Two of the quasars, SDSS J1218+4706 and 1243−0232, are strongly detected; the net source counts for FPMA+B in the 8–24 keV band are 188 and 90, respectively. Figure 2 shows the 8–24 keV no-source probabilities for the three fainter sources, SDSS J0758+3923, 0840+3838, and 1713+5729. Poisson, rather than binomial, no-source probabilities have been adopted for the purposes of the figure only, to aid inter-object comparison; these provide a good approximation of the binomial no-source probabilities (P_B) since the background counts are large (Weisskopf et al. 2007). Although SDSS J0758 +3923 is formally undetected at 8–24 keV, it is only just below the adopted detection threshold for this band and is weakly detected in the broader 3–24 keV energy band, but for FPMA only ($P_B = 0.63\%$). SDSS J0840+3838 is a non-detection. SDSS J1713+5729 is weakly detected with FPMA+B for the 8–24 keV band only ($P_B = 0.22\%$). In general, the detected sources have more net source counts in the 8–24 keV band, where the focusing soft X-ray observatories (e.g., *Chandra* and *XMM-Newton*) have little to no sensitivity, than in the 3–8 keV band, where *NuSTAR* and the soft X-ray observatories overlap. This can occur for heavily obscured AGNs, which have extremely flat X-ray spectra and are therefore brighter at

Table 2
X-Ray Photometry: *NuSTAR* Counts

Object Name	Net Counts (3–24 keV)			Net Counts (3–8 keV)			Net Counts (8–24 keV)		
SDSS J	FPMA	FPMB	FPMA+B	FPMA	FPMB	FPMA+B	FPMA	FPMB	FPMA+B
0758+3923	$30.4^{+17.9}_{-16.4}$	<14.8	<43.8	<29.3	<7.2	<18.1	<30.4	<21.8	<45.0
0840+3838	<25.2	<17.1	<28.4	<14.6	<8.8	<13.4	<19.1	<21.5	<31.5
1218+4706	$122.9^{+20.8}_{-19.3}$	$127.2^{+21.6}_{-20.2}$	$249.9^{+29.5}_{-28.0}$	$32.4^{+12.6}_{-11.1}$	$32.4^{+13.3}_{-11.8}$	$64.7^{+17.8}_{-16.4}$	$91.4^{+17.1}_{-15.6}$	$96.7^{+17.7}_{-16.2}$	$188.0^{+24.1}_{-22.6}$
1243–0232	$56.8^{+19.9}_{-18.4}$	$60.4^{+21.7}_{-20.2}$	$116.9^{+28.9}_{-27.5}$	<32.4	<31.8	$33.8^{+18.8}_{-17.3}$	$40.0^{+15.8}_{-14.3}$	$49.6^{+17.2}_{-15.7}$	$89.6^{+22.8}_{-21.3}$
1713+5729	<43.1	<33.5	<67.4	<18.1	<13.3	<21.5	<33.9	<36.3	$38.1^{+19.6}_{-18.1}$

Note. *NuSTAR* net source counts for the candidate CTQSO2s. FPMA and FPMB are the individual focal plane modules belonging to the two telescopes which comprise *NuSTAR*. "FPMA+B" refers to the combined FPMA+FPMB data.
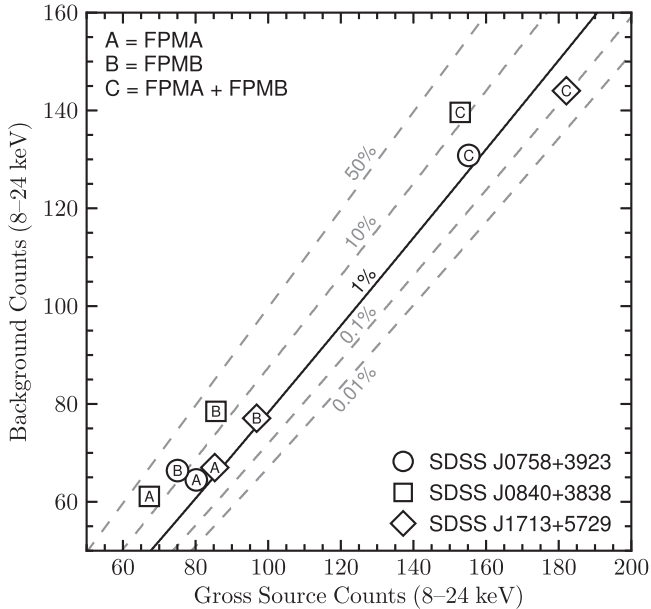

Figure 2. *NuSTAR* photometry at 8–24 keV for the faintest three sources, SDSS J0758+3923, 0840+3838 and 1713+5729 (circles, squares, and diamonds, respectively). Gross source counts and background counts (scaled to the source aperture) are shown. The dashed lines indicate tracks of constant Poisson no-source probability (a good approximation of P_B, given the large background counts considered here; Weisskopf et al. 2007). The solid black line shows our adopted detection threshold of $P_B = 1\%$. Only SDSS J1713+5729 is detected: while it is not detected in the individual FPMs, the increased sensitivity in FPMA+B (i.e., the combined FPMA+FPMB data) results in a significant detection, with $P_B = 0.22\%$.
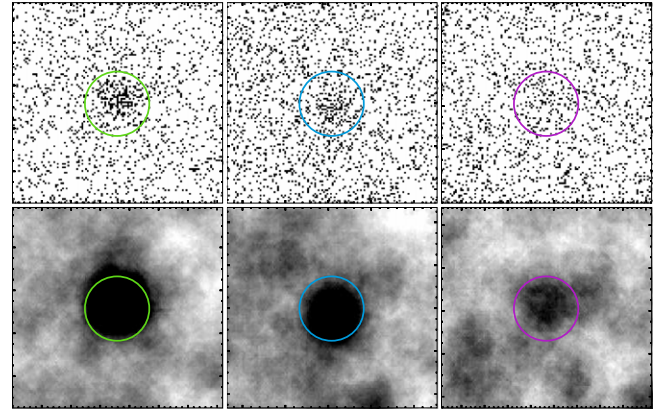

Figure 3. *NuSTAR* 8–24 keV images for the three objects detected in this energy band: SDSS J1218+4706, 1243–0232, and 1713+5729 (left to right, respectively). Top row: unsmoothed photon images. Bottom row: images smoothed with a top hat function of radius 14 pixels, corresponding to 34″5 (for aesthetic purposes only). The 45″ radius source apertures are shown, centered on the SDSS positions. The major tickmarks indicate 1 arcmin offsets in right ascension (R.A.; horizontal axis) and declination (decl.; vertical axis).

$\gtrsim 8$ keV. Indeed, the single candidate CTQSO2 to be detected with *NuSTAR* in L14, SDSS J0011+0056, was only detected in the 8–24 keV band. *NuSTAR* FPMA+B 8–24 keV image cutouts for the three new targets detected in this energy band are shown in Figure 3. None of these three sources are detected in the most sensitive *Swift* BAT all-sky catalogs (e.g., Baumgartner et al. 2013), and direct examination of the 104 month *Swift* BAT maps shows no excess above 2σ (for details of the maps and procedures, see Koss et al. 2013). Therefore, *NuSTAR* has provided the first real detections of these targets at high energies (>10 keV).

For the *NuSTAR*-detected sources, it is important to rule out confusion with and contamination from other nearby X-ray sources. Both of these are extremely unlikely: in the soft X-ray (*Chandra* and *XMM-Newton*) imaging of the *NuSTAR*-detected sources, the only neighboring source detected within 88″ (i.e., the radial distance containing an encircled-energy fraction of ~85% for the *NuSTAR* PSF) of the SDSS positions lies at an

angular separation of 51″ from SDSS J1218+4706 (i.e., outside our adopted source aperture radius) and is a factor of ≈20 fainter in the *XMM-Newton* energy band.

Table 3 lists the aperture-corrected *NuSTAR* fluxes and rest-frame 10–40 keV luminosities ($L_{10-40\,\mathrm{keV}}$; uncorrected for absorption). The fluxes were obtained using photometry, assuming an effective photon index (i.e., for an unabsorbed power law model) of $\Gamma_{\mathrm{eff}} = 0.3$ and using count rate to flux conversion factors which account for the *NuSTAR* response and effective area. Often $\Gamma_{\mathrm{eff}} = 1.8$ (a typical value for the 3–24 keV emission of AGNs; e.g., Alexander et al. 2013) is assumed for such extrapolations, but the *NuSTAR*-detected candidate CTQSO2s have extremely flat observed spectral slopes at 3–24 keV (see Section 4), in agreement with $\Gamma_{\mathrm{eff}} = 0.3$ in all cases. For each object our measured *NuSTAR* flux is in agreement with the soft X-ray observatory (*Chandra* or *XMM-Newton*) measurement at 3–8 keV, the energy band in which the observatories overlap. For the three faint or undetected sources (SDSS J0758+3923, 0840+3838 and 1713+5729), the $L_{10-40\,\mathrm{keV}}$ values were obtained by extrapolating from the observed-frame 8–24 keV fluxes assuming $\Gamma_{\mathrm{eff}} = 0.3$. For the two sources with good *NuSTAR* photon statistics (SDSS J1218+4706 and 1243–0232) the $L_{10-40\,\mathrm{keV}}$ values were calculated using the best-fitting spectral models (Section 4.1).

Table 3
Multiwavelength Flux and Luminosity Measurements

Object	Observed-frame Flux (10^{-13} erg s^{-1} cm^{-2})				Rest-frame Luminosity (10^{42} erg s^{-1})			$\hat{a}$	$\hat{f}_{6\,\mu m}$
	Chandra/*XMM*	*NuSTAR*			*Chandra*/*XMM*	*NuSTAR*		SED Modeling	
SDSS J	3–8 keV	3–8 keV	3–24 keV	8–24 keV	2–10 keV	10–40 keV	6 μm	0.1–30 μm	6 μm
(1)	(2)	(3)	(4)	(5)	(6)	(7)	(8)	(9)	(10)
0758+3923	$0.13^{+0.03}_{-0.02}$	<0.12	<0.69	<0.93	$2.33^{+0.40}_{-0.35}$	<23.22	347 ± 19	0.88 ± 0.01	0.97 ± 0.00
0840+3838	<0.13	<0.09	<0.48	<0.69	<3.93	<35.23	130 ± 10	0.63 ± 0.03	0.73 ± 0.04
1218+4706	$0.57^{+0.05}_{-0.47}$	$0.49^{+0.13}_{-0.12}$	$4.66^{+0.55}_{-0.52}$	$4.49^{+0.58}_{-0.54}$	$1.38^{+0.10}_{-0.12}$	$14.00^{+44.53}_{-1.17}$	73 ± 3	0.91 ± 0.01	0.99 ± 0.01
1243−0232	$0.15^{+0.08}_{-0.09}$	$0.19^{+0.11}_{-0.10}$	$1.65^{+0.41}_{-0.39}$	$1.62^{+0.41}_{-0.39}$	$5.74^{+0.69}_{-0.56}$	$54.60^{+5.22}_{-5.67}$	25 ± 4	0.30 ± 0.04	0.52 ± 0.07
1713+5729	<0.30	<0.12	<0.95	$0.69^{+0.35}_{-0.33}$	<1.07	$4.76^{+2.45}_{-2.26}$	305 ± 21	0.92 ± 0.02	$0.99^{+0.01}_{-0.03}$

Notes. Columns (2)–(7): hard X-ray (*NuSTAR*) and soft X-ray (*Chandra* or *XMM-Newton*) fluxes and luminosities. The rest-frame X-ray luminosities are observed values, i.e., uncorrected for absorption, and are in units of 10^{42} erg s^{-1}. The *NuSTAR* fluxes are from photometry in three observed-frame energy bands, assuming $\Gamma_{\rm eff} = 0.3$. The rest-frame 10–40 keV luminosities are determined from the best-fitting spectral models (Section 4.1) for SDSS J1218+4706 and 1243−0232, and by extrapolating from the observed-frame 8–24 keV band (assuming $\Gamma_{\rm eff} = 0.3$) for SDSS J0758+3923, 0840+3838, and 1713+5729. The *Chandra* and *XMM-Newton* fluxes and luminosities are determined from spectroscopy for SDSS J0758+3923, 1218+4706, and 1243−0232, and from aperture photometry in the observed-frame 3–8 keV and rest-frame 2–10 keV bands for SDSS J0840+3838 and 1713+5729 (assuming $\Gamma_{\rm eff} = 0.3$). Columns (8)–(10): best-fit parameters from the near-UV to mid-IR SED modeling in Section 3.3. The errors shown correspond to standard deviations from a Monte Carlo re-sampling of the photometric data. Column (8): rest-frame 6 μm luminosity for the AGN only, $L_{6\,\mu m}$ (νL_{ν}), in units of 10^{42} erg s^{-1}. This value is intrinsic (i.e., corrected for dust extinction). Column (9): the fractional contribution of the AGN to the total integrated intrinsic luminosity between 0.1 and 30 μm. Column (10): the fractional contribution of the AGN to the observed (i.e., uncorrected for dust extinction) monochromatic rest-frame 6 μm flux.

3.2. Lower Energy X-Ray Data

To incorporate lower energy (<10 keV; or "soft") X-ray data in our study, we use archival *Chandra* and *XMM-Newton* observations, limiting the analysis to the 0.5–8 keV and 0.5–10 keV bands, respectively. Table 1 provides details of the archival soft X-ray observations, including dates and net exposure times. For the sources with poor photon statistics, we perform photometry using procedures identical to those for the *NuSTAR* photometry (see Section 3.1). For the sources with good photon statistics, we model the X-ray spectra with XSPEC (see Section 4.1). As mentioned in Section 3.1, source confusion is extremely unlikely: there are no neighboring sources detected within 51″ of the QSO2 positions. Measurements of the observed-frame 3–8 keV fluxes and rest-frame 2–10 keV luminosities (uncorrected for absorption) are listed in Table 3.

For the source with *Chandra* coverage (SDSS J1243−0232), we process the data using CHANDRA_REPRO.[28] The source events are extracted from a circular 2″.5 radius aperture. The background events are extracted from a background source-free annulus centered on the source coordinates, with an inner radius of 8″ and an outer radius of 80″. Since SDSS J1243−0232 is on-axis, a large fraction ($\gtrsim$90%) of the source counts lie within the source aperture. Given this, and the extremely low net source counts measured (9), contamination of the background region by source counts is negligible.

For the sources with *XMM-Newton* coverage, we analyze data products from the Pipeline Processing System using the *Science Analysis Software* (SAS v.13.5.0). To determine appropriate count rate thresholds for background flare subtraction, we visually examine the light curves. In all cases the fraction of exposure time removed is $\leqslant$30%, except in the case of obsID 0305750401 where the fraction is 49%. The exposure times in Table 1 are flaring-corrected. The source events are extracted from circular regions of 8″–20″ radius (depending on source brightness and off-axis angle). The background events are extracted from regions of area 70″ × 70″ to 140″ × 140″,

using either an annulus centered on the source position or an offset region if it is necessary to avoid chip gaps or nearby sources. We combine the MOS1 and MOS2 data using the SAS task EPICSPECCOMBINE, and simultaneously fit the PN and MOS data when performing spectral analyses.

In the case of SDSS J1218+4706, we use the two archival *XMM-Newton* observations with the longest exposures and most recent start dates (obsIDs 0203270201 and 0400560301). For obsID 0203270201, SDSS J1218+4706 lies close to the on-axis position. In this instance we only use the MOS data, since the source lies on a chip gap for PN. For obsid 0400560301, SDSS J1218+4706 lies far off-axis. In this case we only use the PN data since the source lies on a chip edge in MOS1 and there are relatively low net counts with MOS2 (65).

3.3. Near-UV to Mid-IR SED Analysis

Here we analyze near-UV to mid-IR (0.3–30 μm) SEDs for the five candidate CTQSO2s presented in this work, and the one presented in G14 (SDSS J1034+6001), with the primary aim of reliably measuring the AGN emission at mid-IR wavelengths. The photometric data (shown in Figure 4) are collated from the SDSS (Data Release 7; York et al. 2000), the *WISE* All-Sky source catalog (Wright et al. 2010), and the *Spitzer* (Werner et al. 2004) Enhanced Imaging Products Source List (for SDSS J1243−0232 only). The SDSS fluxes are corrected for Galactic extinction. The photometric data adopted are provided in the Appendix. In order to provide a consistent SED analysis across the full sample of nine *NuSTAR*-observed candidate CTQSO2s, we use the same SED decomposition procedure as that which was applied to the initial three objects in L14. Following the methodology detailed in Assef et al. (2008, 2010, 2013), each SED is modeled as the best-fit, non-negative, linear combination of four empirical templates (Assef et al. 2010), including one AGN template and three galaxy templates for: an old stellar population ("elliptical" or E), ongoing star formation ("spiral" or Sbc), and a starburst population ("irregular" or Im). The internal dust extinction of the AGN component is included as a free parameter in the modeling. The model solutions are shown in Figure 4, and the

---

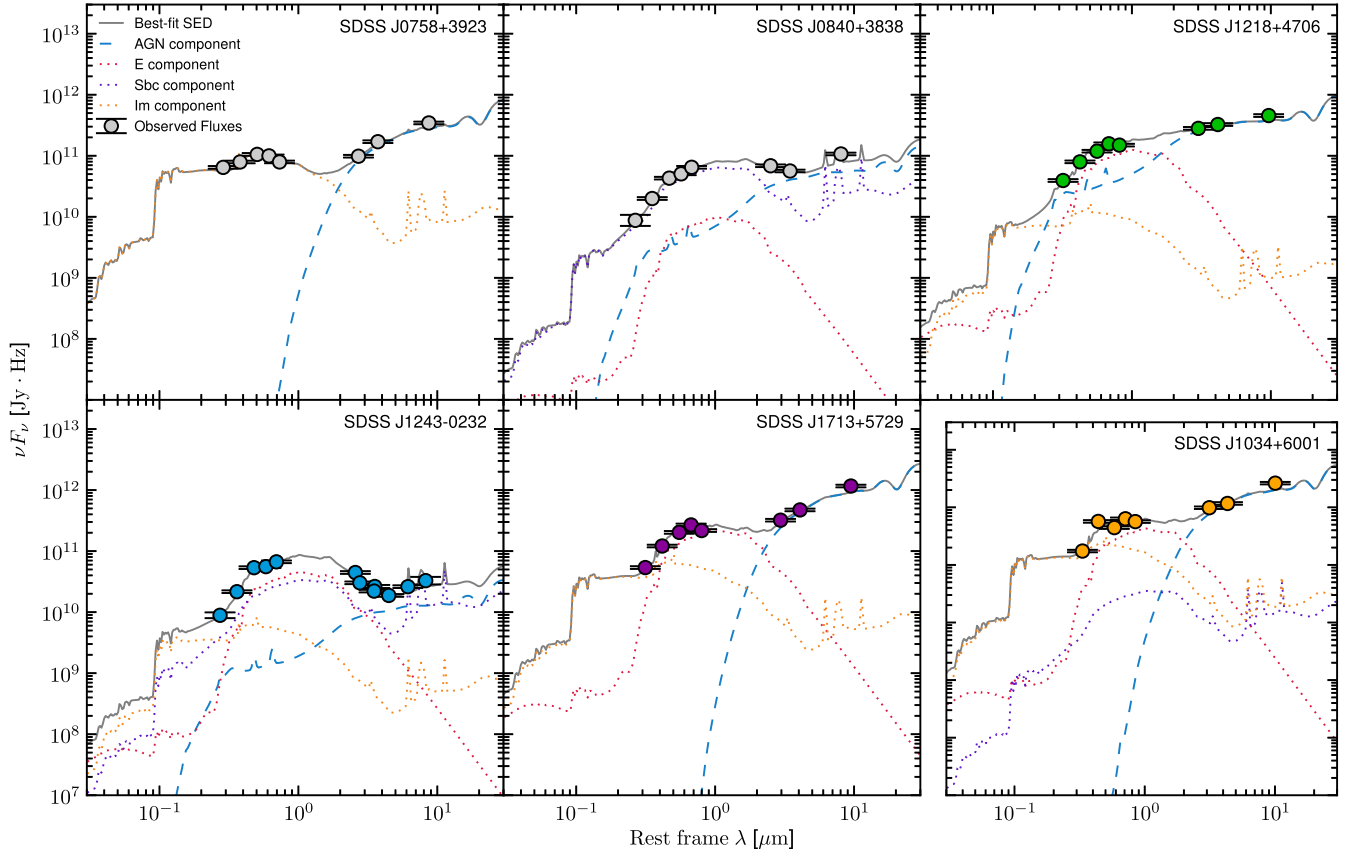[28] http://cxc.harvard.edu/ciao/ahelp/chandra_repro.html

Figure 4. Near-UV to mid-IR spectral energy distributions (SEDs) for the five candidate CTQSO2s presented in this work and the one (SDSS J1034+6001) presented in G14. AGN (blue dashed curve) and galaxy (dotted curves) templates were combined in the best-fit modeling of the photometric data (colored circles for the sources detected at 8–24 keV with *NuSTAR* and gray circles for the 8–24 keV non-detections) following Assef et al. (2008, 2010, 2013). The three galaxy templates correspond to an old stellar population ("elliptical" or E; red), ongoing star formation ("spiral" or Sbc; purple), and a starburst population ("irregular" or Im; orange). The gray curve shows the combined model solution. The systems are all AGN-dominated in the mid-IR waveband based on this analysis, except for SDSS J1243−0232, which has comparable contributions from the AGN and the host galaxy; see Table 3.

following best-fitting parameters are listed in Table 3: $\hat{a}$, the fractional contribution of the AGN to the total intrinsic (i.e., corrected for the dust extinction of the AGN component) integrated 0.1–30 μm luminosity, $\hat{f}_{6\,\mu m}$, the fractional contribution of the AGN to the total observed (i.e., uncorrected for the dust extinction of the AGN component) monochromatic rest-frame 6 μm flux, and $L_{6\,\mu m}$, the intrinsic AGN luminosity at rest-frame 6 μm (νL_ν). The errors represent standard deviations from a Monte Carlo re-sampling of the photometric data over 1000 iterations and thus account for possible model degeneracies. In all cases the integrated light properties (i.e., the total galaxy and AGN contributions) are well constrained, which is required to accurately determine $\hat{a}$, $\hat{f}_{6\,\mu m}$, and $L_{6\,\mu m}$. Since the primary goal of the SED modeling was to reliably measure these parameters, we do not make inferences about the host galaxy properties from the best-fit combination of host galaxy templates. SDSS J1034+6001, not shown in Table 3 since the X-ray analysis is presented in G14, has $L_{6\,\mu m} = (1.20 \pm 0.09) \times 10^{44}$ erg s^{-1}, $\hat{a} = 0.90 \pm 0.02$, and $\hat{f}_{6\,\mu m} = 0.98^{+0.02}_{-0.03}$.

The $\hat{a}$ constraints demonstrate that the candidate CTQSO2s in Figure 4 require an AGN component at a very high CL, and that in general the AGN contributes strongly to the intrinsic emission across the broad 0.1–30 μm wavelength range (all but one object have $\hat{a} \gtrsim 0.6$). The high $\hat{f}_{6\,\mu m}$ values (all but one

have $\hat{f}_{6\,\mu m} \gtrsim 0.7$) indicate that the observed monochromatic 6 μm fluxes are AGN-dominated. The presence of an AGN at mid-IR wavelengths may also be inferred using *WISE* color diagnostics. In Figure 5 we show the six objects from Figure 4, and the three from L14, on the *WISE* W1−W2 (i.e., [3.4 μm]–[4.6 μm]) versus W2−W3 (i.e., [4.6 μm]–[12.0 μm]) plane. Generally, sources with larger W1−W2 values have stronger AGN contributions. We compare our findings with the AGN "wedge" of Mateos et al. (2013) and the W1−W2 color cut of Stern et al. (2012), which may be used to identify AGN-dominated systems. Out of the total sample of nine candidate CTQSO2s, five are AGN-dominated according to both criteria, and one (SDSS J0056+0032) falls below the Mateos et al. (2013) wedge but lies above the Stern et al. (2012) cut. This is in good agreement with the SED modeling for these sources, where $\hat{a} \gtrsim 0.9$ in all cases. The remaining three sources (SDSS J0011+0056, 0840+3838 and 1243−0232) fall below both of the selection regions, although SDSS J0840+3838 is consistent with satisfying the Stern et al. (2012) AGN selection criterion given the errors. This supports the SED modeling, from which it is concluded that these three sources are the least AGN-dominated ($\hat{a} \approx 0.3$–0.6 and $\hat{f}_{6\,\mu m} \approx 0.5$–0.7). The *WISE* colors of the objects agree with the expectations; in general, the CTQSO2 population appears to follow the *WISE* color distribution of the total QSO2 population, with a fraction of objects (∼70%) lying within the AGN wedge (Mateos
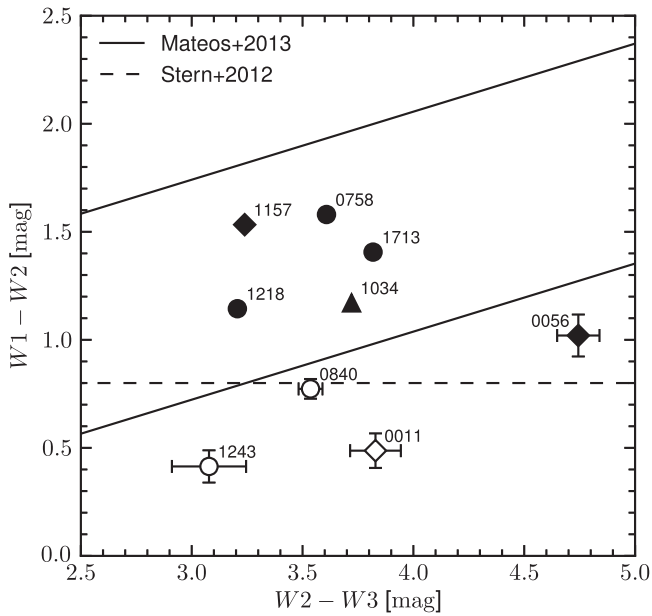
Figure 5. *WISE* color–color diagram for the *NuSTAR*-observed SDSS-selected candidate CTQSO2s from this study (circles), G14 (triangle), and L14 (diamonds). We compare these with the AGN color cut of Stern et al. (2012; $W1 - W2 \geqslant 0.8$) and the AGN "wedge" of Mateos et al. (2013). The filled and empty symbols mark sources that are strongly AGN-dominated ($\hat{a} \gtrsim 0.9$) and less AGN-dominated ($\hat{a} \lesssim 0.6$), respectively, at mid-IR wavelengths according to our SED modeling. For the five objects that lie within the AGN wedge, the error bars are smaller than the symbols.

et al. 2013). In the local universe, $\sim 40\%$ of the currently known bona fide CT AGNs lie within the wedge (Gandhi et al. 2015).

In addition to the near-UV to mid-IR SED, one of the candidate CTQSO2s presented in this work (SDSS J1713 +5729) has a detection at far-IR wavelengths with *IRAS* that allows us to assess the extent to which star formation could contribute to the soft X-ray emission (Section 4.1.3).

4. RESULTS

To summarize the *NuSTAR* source detection for the five SDSS-selected candidate CTQSO2s presented in this work: two are strongly detected, one is weakly detected, and two are undetected by *NuSTAR* in the high-energy band (8–24 keV). In Section 4.1 we present the results of X-ray spectral fitting with XSPEC for the three brightest objects. In Section 4.2 we present the X-ray band ratios of all of the *NuSTAR*-detected candidate CTQSO2s, compared to model predictions. For the weakly detected source SDSS J1713+5729, this is an appropriate method for characterizing the broad-band X-ray spectrum. These two sections give *direct* (i.e., X-ray spectral) constraints on absorbing column densities ($N_{\rm H}$). In Section 4.3, we present *indirect* constraints from a multiwavelength diagnostic for the entire sample, including *NuSTAR* non-detections.

First we take a brief look at the overall X-ray spectral shapes for the full sample of nine *NuSTAR*-observed candidate CTQSO2s. Figure 6 shows the effective photon indices ($\Gamma_{\rm eff}$), measured through unabsorbed power law fits to the individual *Chandra* or *XMM-Newton* (0.5–8 keV) and *NuSTAR* (3–24 keV) spectra. The spectral shapes observed by *Chandra* and *XMM-Newton* vary significantly over an order of magnitude in the (non-absorption-corrected) rest-frame 2–10 keV luminosity. The increase in $\Gamma_{\rm eff}$ (0.5–8 keV) toward
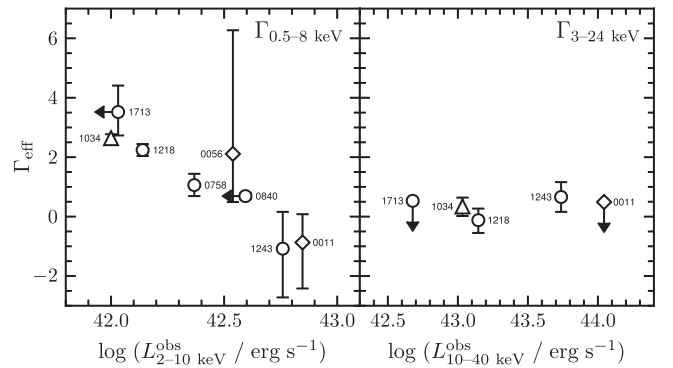

Figure 6. Observed X-ray properties of the *NuSTAR*-observed candidate CTQSO2 sample. Left panel: properties measured at low energies with *Chandra* and *XMM-Newton*. Right panel: properties measured at high energies with *NuSTAR*. Only detected sources are shown. Circles, diamonds, and the triangle indicate the objects presented in this work, L14, and G14, respectively. The effective photon index ($\Gamma_{\rm eff}$), which provides a basic description of the overall X-ray spectral shape, was obtained by fitting an unabsorbed power law model to the data for each source. The rest-frame X-ray luminosities ($L_{\rm X}^{\rm obs}$; bottom axis) are observed values, i.e., uncorrected for absorption. For the five objects presented in this paper, the luminosities correspond to those in Table 3. For the L14 and G14 objects the luminosities have been calculated using the same methodology: spectral analysis where possible or photometry following the procedure outlined in Section 3.1. In the cases of the X-ray faint sources SDSS J0011+0056 and SDSS J1713+5729, the $\Gamma_{\rm eff}$ for 3–24 keV was estimated from the *NuSTAR* band ratio (BR$_{\rm Nu}$; see Section 4.2).

lower luminosities may reflect an increase in the relative contribution to the low-energy spectra from processes unrelated to direct AGN emission, such as thermal plasma emission due to star formation or AGN-powered photoionization. In contrast, the spectra seen by *NuSTAR* are consistent with having the same effective photon index: excluding upper limits, the mean is $\Gamma_{\rm eff}$ (3–24 keV) ≈ 0.3.

4.1. X-Ray Spectral Analysis: Best-fit Modeling

Here we use broad-band X-ray spectral modeling for the two brightest *NuSTAR*-detected sources presented in this paper (SDSS J1218+4706 and SDSS J1243−0232) to measure intrinsic properties: the intrinsic absorbing column density ($N_{\rm H}$), the intrinsic photon index (Γ), and the intrinsic X-ray luminosity ($L_{\rm X}$). Additionally, we investigate the low-energy X-ray spectrum of SDSS J1713+5729. The X-ray spectral fitting is performed using XSPEC version 12.8.1j (Arnaud 1996). In all cases we account for Galactic absorption using a PHABS multiplicative component, with column densities fixed at values from Kalberla et al. (2005).

4.1.1. SDSS J121839.40+470627.7

SDSS J1218+4706 has the strongest *NuSTAR* detection in the 8–24 keV band, with net source counts of $S_{8-24\,{\rm keV}} = 188$ for FPMA+B. The *NuSTAR* data are complemented by relatively high quality soft X-ray data, with two long *XMM-Newton* exposures (obsIDs 0203270201 and 0400560301; see Table 1). Below we analyze the broad-band (0.5–24 keV) *NuSTAR* plus *XMM-Newton* data set (shown in Figure 7). The modeling approach taken is similar to that adopted by G14 for SDSS J1034+6001, the other brightest source in the *NuSTAR*-observed QSO2 sample, which has comparable photon statistics ($S_{8-24\,{\rm keV}} = 182$). We group the data by a minimum of 20 counts per bin, and use χ^2 minimization (statistic chi in XSPEC) to constrain parameters. We note
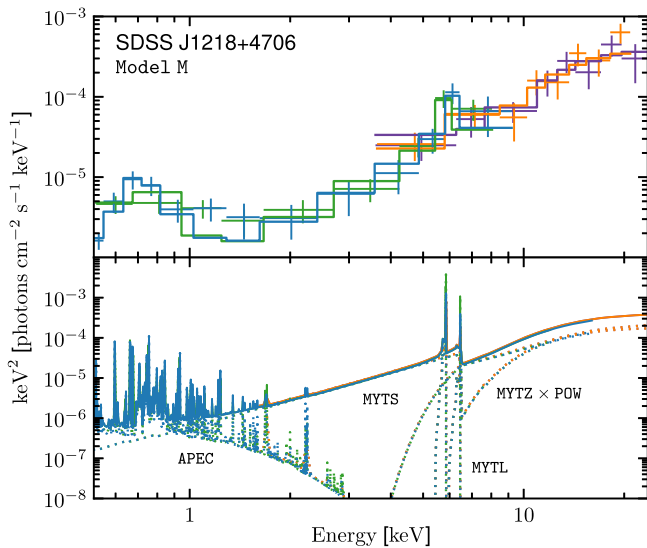
Figure 7. Unfolded *NuSTAR* plus *XMM-Newton* spectrum, in EF_E units, for SDSS J1218+4706. The data are shown in the upper panel, grouped to a minimum significance of 2σ per bin for visual purposes. The *NuSTAR* FPMA and FPMB data are shown in purple and orange, respectively. The MOS (obsID 0203270201) and PN (obsID 0400560301) data are shown in green and blue, respectively. The best-fit MYTORUS-based model (Model M; described in Section 4.1.1) is shown binned to match the data (solid lines, upper panel) and in full detail (lower panel).

that using statistic cstat instead (applying the W statistic approach; e.g., see Section 4.1.2) results in essentially unchanged values for the key best-fit parameters (Γ and N_H change by less than 0.1 and 0.1×10^{24} cm^{-2}, respectively, for the models tested). The *XMM-Newton*:*NuSTAR* cross-normalization factor, when left as a free parameter, converges to slightly different values depending on the model being tested, but is always broadly consistent (given the uncertainties) with the current best calibration measurements of Madsen et al. (2015) of $\approx$0.93. We therefore fix the cross-normalization factor to this value throughout.

As shown in Figure 6, SDSS J1218+4706 has an extremely flat effective photon index over the *NuSTAR* band, $\Gamma_{3-24\,\mathrm{keV}} = -0.15^{+0.40}_{-0.45}$. This is indicative of a spectrum dominated by Compton reflection, as a result of the primary continuum being heavily suppressed by CT levels of photo-electric absorption (e.g., George & Fabian 1991). Another important diagnostic feature of reflection is fluorescent Fe Kα line emission, which occurs at rest-frame 6.4 keV and becomes increasingly prominent as the level of absorption increases (e.g., Risaliti 2002). An equivalent width threshold of EW$_{\mathrm{Fe\,K}\alpha} > 1\,\mathrm{keV}$ is commonly used to identify CT AGNs; such high values are difficult to explain for less than CT columns (e.g., Maiolino et al. 1998; Comastri 2004) and suggest a heavily reflection-dominated or pure reflection spectrum, where little to none of the directly transmitted AGN emission is visible.

For SDSS J1218+4706, there is a clear excess of emission at observed frame $\approx$6 keV, which has previously been interpreted as Fe Kα line emission (J13; LaMassa et al. 2012). To model this, we fit to the $>$2 keV *NuSTAR* plus *XMM-Newton* data set an unobscured power law and Gaussian component, fixing the line energy at $E_{\mathrm{line}} = 6.4$ keV and the line width at $\sigma_{\mathrm{line}} = 0.01$ keV. We measure an observed-frame equivalent width of

EW$_{\mathrm{Fe\,K}\alpha} = 1.7^{+0.7}_{-0.6}$ keV using the *XMM-Newton* spectra. This value is similar to but more tightly constrained than that published by J13 since they only use one of the archival *XMM-Newton* observations while we use two here. The Fe Kα line equivalent width is above the commonly adopted threshold for CT AGNs (EW$_{\mathrm{Fe\,K}\alpha} > 1$ keV), with a value comparable to that of the CT quasar SDSS J1034+6001 (Mrk 34; G14). Freeing the Gaussian line energy parameter, we obtain a best-fit value of $E_{\mathrm{line}} = 6.40^{+0.24}_{-0.07}$ keV (rest frame), which adds further confidence that the excess emission is due to Fe Kα.

For the X-ray spectral modeling of SDSS J1218+4706, we first conduct a simple test to assess the nature of the AGN continuum; we fit the 7–24 keV *NuSTAR* data with two extreme models: one reflection-only spectrum and one transmission-only spectrum. Fitting the high-energy data above 7 keV allows a clean measurement of the AGN continuum *independent* of how the potentially complex lower energy emission is chosen to be modeled; low-energy X-ray emitting processes other than the reflected or directly transmitted AGN continuum can dominate up to energies of $\approx$4 keV (e.g., Gandhi et al. 2014, 2015), and fluorescent line emission (e.g., Fe Kα) can also strongly contribute at energies up to $\approx$7 keV. For the reflection-only model we use PEXRAV (Magdziarz & Zdziarski 1995), with the reflection scaling factor set to -1 to produce a reflection-only spectrum (i.e., no directly transmitted component), and set all other parameters to the default values. This model provides a statistically acceptable fit to the *NuSTAR* data ($\chi^2/n = 11.3/12$; here, n is the number of degrees of freedom), and the intrinsic photon index is constrained to be $\Gamma = 1.35 \pm 0.46$. For the transmission-only model we use CABS · ZWABS · POW (in XSPEC formalism).[29] It is not possible to simultaneously constrain N_H and Γ in this case, so we fix the intrinsic photon index at $\Gamma = 1.8$ (a typical value for AGNs detected by *NuSTAR* at 3–24 keV; e.g., Alexander et al. 2013). Again, there is a statistically acceptable fit to the data ($\chi^2/n = 10.5/12$) for a best-fit column density of $N_H = (1.9^{+0.7}_{-0.5}) \times 10^{24}$ cm^{-2}.

The above tests support the empirical evidence (from Γ_{eff} and EW$_{\mathrm{Fe\,K}\alpha}$) that extremely large, CT column densities are required to explain the X-ray spectrum of SDSS J1218 +4706. In the most extreme case, the source is consistent with being fully reflection-dominated (no directly transmitted component), which would imply $N_H \gg 1.5 \times 10^{24}$ cm^{-2}. In the least extreme case, the source is consistent with lying close to the CT threshold ($N_H \approx 1.5 \times 10^{24}$ cm^{-2}). However, the latter model assumes a transmission-only spectrum (no Compton reflection), which is unlikely given the large measured equivalent width of Fe Kα. The reflection-only model tested (PEXRAV) is also limited in that the geometry (a slab of material) and infinite optical depth assumed are not well motivated for obscured AGNs. Ideally, in the CT regime, any absorbed continuum, reflected continuum, and fluorescent lines should be modeled in a self-consistent way and assuming a well motivated geometry. This is possible using the physical models MYTORUS (Murphy & Yaqoob 2009) and BNTORUS (Brightman & Nandra 2011), which were produced using

---

[29] The model PLCABS (Yaqoob 1997) is generally a preferable transmission model to use (over CABS · ZWABS · POW) for column densities of $N_H >$ few $\times 10^{23}$ cm^{-2}. However, in our case PLCABS is not appropriate since the energy range for which the model is valid depends on source column density ($E < 14.4$ keV for $N_H \leqslant 10^{24}$ cm^{-2}; $E < 10$ keV for $N_H \leqslant 5 \times 10^{24}$ cm^{-2}; Yaqoob 1997), which means not utilizing the high-energy *NuSTAR* data.

Table 4
Best-fit Models for the *NuSTAR* + *XMM-Newton* Spectrum
of SDSS J1218+4706

	Model M	Model T
χ^2/n	31.9/38	33.0/39
Γ	$2.4^{+0.2}_{-0.3}$	$2.8^{+u}_{-0.4}$
N_H (10^{24} cm^{-2})	$2.0^{+u}_{-0.8}$	$2.2^{+1.2}_{-0.6}$
θ_{tor} (°)	[60.0]	[60.0]
θ_{inc} (°)	$63.7^{+8.5}_{-2.9}$	[87.0]
kT_{APEC} (keV)	$0.42^{+0.20}_{-0.11}$	$0.25^{+0.07}_{-0.05}$
$L^{APEC}_{0.5-2keV}$ (10^{41} erg s^{-1})	1.38	1.65
$L^{obs}_{2-10keV}$ (10^{44} erg s^{-1})	0.01	0.01
$L^{obs}_{10-40keV}$ (10^{44} erg s^{-1})	0.14	0.13
$L^{int}_{2-10keV}$ (10^{44} erg s^{-1})	0.85	1.70
$L^{int}_{10-40keV}$ (10^{44} erg s^{-1})	0.46	0.48

Notes. Best-fitting model parameters for the 0.5–24 keV spectrum of SDSS J1218+4706. The individual models are detailed in Section 4.1.1. The column densities (N_H) quoted are defined along the line of sight of the observer.

Monte Carlo simulations of X-ray radiative transfer through toroidal distributions of gas with the two models assuming different toroidal geometries. We proceed to analyze the broad-band (0.5–24 keV) *XMM-Newton* plus *NuSTAR* spectrum of SDSS J1218+4706 using these two models.

Our MYTORUS-based model (Model M hereafter) has the following form:

```
Model M
= PHABS × (MYTZ × POW + MYTS + MYTL + APEC).
```

Here, MYTZ reprocesses the zeroth-order transmitted continuum (POW) through photoelectric absorption and the Compton scattering of X-ray photons out of the line of sight, MYTS is the scattered/reflected continuum produced by scattering X-ray photons into the line of sight, and MYTL is the fluorescent emission line spectrum (Murphy & Yaqoob 2009). We use MYTORUS in the simplest form possible, tying the common parameters of MYTZ, MYTS, and MYTL (N_H and θ_{inc}) together. The intrinsic (unprocessed) photon indices and normalizations are tied to those of the zeroth-order continuum (POW). The torus opening angle (θ_{tor}) is fixed at 60° in the current version of MYTORUS. APEC is a thermal plasma component (Smith et al. 2001) which we use to parameterize the low-energy excess, fixing the abundance parameter at solar. This component is motivated by the steep spectral slope at low energies ($\Gamma_{0.5-2\,keV} \approx 3.4$, measured using an unabsorbed power law model), which suggests contributions from processes such as star formation or AGN photoionization, although we lack the spectral detail required to distinguish between these processes. The best-fit model has $\chi^2/n = 32/38$ (see Table 4 for the model parameters and Figure 7 for the model spectrum). Since Γ and N_H are known to be degenerate, we compute their uncertainties from χ^2 contours in the Γ–N_H plane. Contours showing the 68%, 90%, and 99% confidence regions for this parameter space are shown in Figure 8. These were computed with θ_{inc} left free to vary. Hereafter, the quoted uncertainties for N_H and Γ are taken from the 90% CL contours. The best-fit intrinsic photon index and line of sight column density are $\Gamma = 2.4^{+0.2}_{-0.3}$ and $N_H = (2.0^{+u}_{-0.8}) \times 10^{24}$
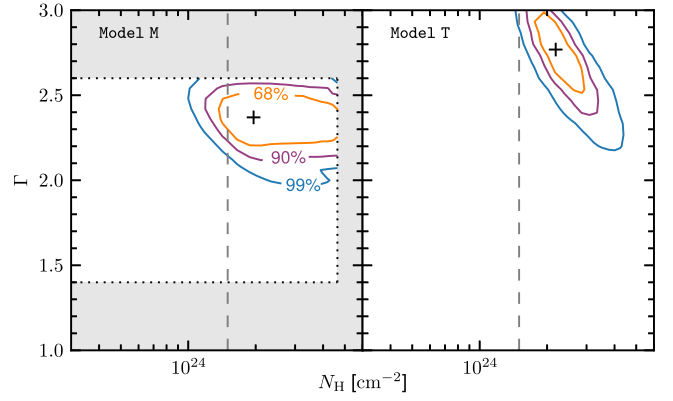

Figure 8. Intrinsic photon index (Γ) vs. (line of sight) column density (N_H) confidence contours for SDSS J1218+4706. The contours outline the 68%, 90%, and 99% confidence regions, and the best-fit value is marked by a black cross. We show results for two models (Model M and Model T; left and right panels). The individual models are detailed in Section 4.1.1. The gray shaded region indicates the parameter ranges for which Model M is not valid. The best-fit column densities are CT ($N_H > 1.5 \times 10^{24}$ cm^{-2}), and the 90% CL lower N_H limits lie just below and just above the CT threshold (gray dashed line) for Model M and Model T, respectively.

cm^{-2} (corresponding to an equatorial column density of $N_{H,eq} = (4.2^{+u}_{-0.8}) \times 10^{24}$ cm^{-2}) for the best-fit inclination angle of $\theta_{inc} = 63°.7^{+8.5}_{-2.9}$. The modeling will not allow inclination angles of $\theta_{inc} < 60°$ since for these angles the observer has a direct, unobscured view of the central X-ray emitting source. The upper error on N_H is not constrained, which is in part due to the limited N_H range of MYTORUS ($N_H = 10^{22}$–10^{25} cm^{-2}). The best-fit model spectrum is reflection-dominated with the MYTS component dominating at $\approx$3–10 keV and the MYTZ and MYTS contributing equally to the normalization and spectral shape at $\gtrsim$10 keV. To assess whether the *NuSTAR* plus *XMM-Newton* spectrum is in agreement with being fully reflection-dominated, we test two modifications of Model M where the MYTZ · POW component is removed and the inclination angle of the MYTS component is set to 0° and 90°, corresponding to face-on and edge-on reflection. Both models provide statistically acceptable fits to the spectrum ($\chi^2/n = 29/35$ and 28/35, respectively), with flat χ^2 residuals, reasonable best-fit intrinsic photon indices ($\Gamma = 1.6^{+0.6}_{-u}$ and 1.9^{+u}_{-u}, respectively) and large column densities for the reflecting material ($N_{H,reflector} = (3.1^{+u}_{-1.6})$ and $(1.5^{+1.0}_{-0.8}) \times 10^{24}$ cm^{-2}, respectively). The broad-band X-ray spectrum of SDSS J1218+4706 is therefore in agreement with being fully reflection-dominated. Since no transmission component is required in these models, we may infer that the line of sight column density is consistent with having a value of $N_H \gg 1.5 \times 10^{24}$ cm^{-2}.

Our BNTORUS-based model (Model T hereafter) has the following form:

```
Model T = PHABS × (BNTORUS + APEC).
```

In the BNTORUS model, N_H is defined along the line of sight, and is independent of θ_{inc}. Initially, we fix the inclination at the maximum value of $\theta_{inc} = 87°$, corresponding to an edge-on view of the torus. Since the opening angle for Model T is poorly constrained when left as a free parameter ($\theta_{tor} < 72°$),

we fix it to $60°$. The best-fit model has $\chi^2/n = 33/39$ (the model parameters are listed in Table 4, and the Γ–N_H contours are shown in Figure 8). N_H is well constrained at the 90% CL, with a best-fit value of $(2.2^{+1.2}_{-0.6}) \times 10^{24} \, cm^{-2}$, and the intrinsic photon index has a relatively high value of $\Gamma = 2.8^{+u}_{-0.4}$. The upper error on Γ is not constrained due to the parameter limits of the BNTORUS model. Fixing the intrinsic photon index at a more reasonable value of $\Gamma = 2.3$, which is consistent with the χ^2 contours and is at the upper end of the range typically observed for unobscured AGNs (e.g., Mateos et al. 2010; Scott et al. 2011) results in a higher column density of $N_H = (3.6^{+0.8}_{-0.7}) \times 10^{24} \, cm^{-2}$ and a reduced χ^2 value close to unity ($\chi^2/n = 39/40$). If the intrinsic photon index is fixed at $\Gamma = 1.8$, an extremely high column density of $N_H > 5.1 \times 10^{24} \, cm^{-2}$ is required. We note that the modeling (with Γ left free) allows a large range of inclination angles ($\theta_{inc} > 63°$), and re-modeling with θ_{inc} fixed at a lower value of $65°$ results in a similarly good fit ($\chi^2/n = 38/39$) with no significant change in N_H but a flatter photon index of $\Gamma = 2.5^{+0.3}_{-0.4}$. Furthermore, the statistical quality of the fit and the best-fit parameters are relatively unchanged when θ_{tor} is left as a free parameter.

To summarize, CT line of sight column densities are preferred for all of the models tested for SDSS J1218+4706. The broad-band X-ray spectrum shows evidence for having a dominant contribution from Compton reflection, with the primary continuum being heavily suppressed due to photo-electric absorption. This is in agreement with the expectations from the observation of strong fluorescent Fe Kα line emission (EW$_{Fe\,K\alpha} \approx 1.7 \, keV$). The lowest limit allowed by the modeling for the line of sight column density is $N_H > 1.2 \times 10^{24} \, cm^{-2}$, and there is no constraint at the upper end. The N_H, L_X and EW$_{Fe\,K\alpha}$ constraints and data quality for SDSS J1218 +4706 ($z = 0.094$) are remarkably similar to those for the other low redshift QSO2 strongly detected by *NuSTAR*, SDSS J1034+6001 ($z = 0.051$; also known as Mrk 34), which was identified by G14 as a bona fide CT AGN. More complex models are possible (such as a clumpy torus; e.g., Bauer et al. 2014), but testing these is beyond the X-ray data quality.

4.1.2. SDSS J124337.34–023200.2

SDSS J1243–0232 is the third brightest *NuSTAR* detection in the SDSS-selected candidate CTQSO2 sample, after SDSS J1218+4706 (Section 4.1.1) and SDSS J1034+6001 (G14), but still has relatively low photon counts: $S_{8-24\,keV} \approx 90$ and $S_{3-8\,keV} \approx 34$ with *NuSTAR*, and $S_{0.5-8\,keV} \approx 9$ with *Chandra*. This emphasizes the challenge involved in studying these inherently faint X-ray sources. Due to the low photon statistics, we use `statistic cstat` in XSPEC, which is more appropriate than `statistic chi` in the case of Poisson distributed data (Nousek & Shue 1989). In the case of unmodeled background spectra, `cstat` applies the W statistic (Wachter et al. 1979).[30] While the W statistic is intended for unbinned data, bins containing zero counts can lead to erroneous results,[31] so we group the *Chandra* and *NuSTAR* data by a minimum of 1 count and 3 counts per bin,

---

[30] See also http://heasarc.gsfc.nasa.gov/docs/xanadu/xspec/wstat.ps
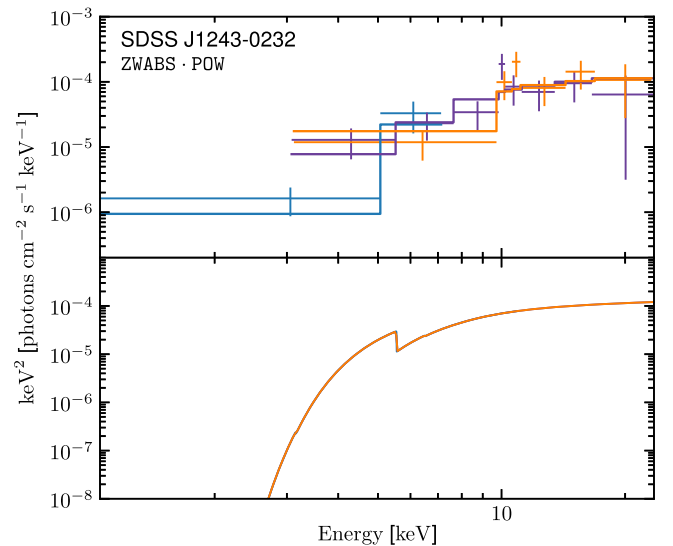[31] See https://heasarc.gsfc.nasa.gov/xanadu/xspec/manual/XSappendixStatistics.html

Figure 9. Unfolded *NuSTAR* (purple and orange for FPMA and FPMB, respectively) plus *Chandra* (blue) X-ray spectrum for SDSS J1243–0232. The best-fit absorbed power law (ZWABS · POW) model is shown. The panel layout, units, and data binning follow that of Figure 7.

respectively (e.g., Wik et al. 2014). We fix the *Chandra*: *NuSTAR* cross-normalization factor at 1.0, consistent with the value obtained when the cross-normalization factor is left as a free parameter in the modeling.

The *NuSTAR* spectrum of SDSS J1243–0232 has a flat effective photon index of $\Gamma_{3-24\,keV} = 0.66 \pm 0.50$, indicative of heavy absorption. Fitting the broad-band (0.5–24 keV) *NuSTAR* plus *Chandra* spectrum with a simple absorbed power law (ZWABS · POW) model, we obtain $N_H \approx 1.6 \times 10^{24} \, cm^{-2}$ and $\Gamma \approx 3$. This intrinsic photon index is discrepant with the expected range for AGNs, and the parameter is poorly constrained. We therefore fix the parameter to $\Gamma = 1.8$ (typical value in the 3–24 keV energy band for AGNs; e.g., Alexander et al. 2013). The best-fitting model has $\chi^2 = 101$ and a C statistic value of $C = 123$, for $n = 130$. The unfolded spectrum and best-fitting model are shown in Figure 9. The column density, $N_H = (0.90^{+0.36}_{-0.33}) \times 10^{24} \, cm^{-2}$, is close to CT. The intrinsic luminosities in the low and high-energy X-ray bands are $L^{in}_{2-10\,keV} = 0.6 \times 10^{44} \, erg \, s^{-1}$ and $L^{in}_{10-40\,keV} = 0.7 \times 10^{44} \, erg \, s^{-1}$, respectively. The higher quality *NuSTAR* data dominate the fit, with similar results [$N_H = (0.97^{+0.49}_{-0.38}) \times 10^{24} \, cm^{-2}$] being obtained when the *Chandra* data are excluded. We note that `cstat` may also be used to model the unbinned, gross (i.e., combined source plus background) spectrum, in which case the Cash statistic (C statistic; Cash 1979) is applied. Characterizing the background spectra using double power law models (POW + POW in XSPEC) and including these as fixed components in the spectral modeling of the *NuSTAR* data, this C statistic approach yields results very similar to those of the W statistic approach, with $N_H = (0.97^{+0.46}_{-0.37}) \times 10^{24} \, cm^{-2}$.

Given the extremely flat effective photon index measured for this source, it is reasonable to test whether the spectrum is in agreement with a pure reflection continuum. As in Section 4.1.1, we use PEXRAV with the reflection scaling factor set to -1 to produce a reflection-only spectrum. The model produces a similarly good fit to the data as for the absorbed power law model above, with $\chi^2 = 117$ and $C = 120$, for

$n = 130$. We infer that the line of sight column density is consistent with being CT, with $N_H \gg 1.5 \times 10^{24}$ cm^{-2}. Unlike for the absorbed power law model, the intrinsic photon index is well constrained by the reflection-only model, with $\Gamma = 1.7 \pm 0.3$. To summarize, the *NuSTAR* data unambiguously reveal heavy absorption in this QSO2, with a column density lower limit of $N_H > 0.6 \times 10^{24}$ cm^{-2} and no constraint at the high, CT absorption end. Higher quality X-ray data than those currently available, especially at <10 keV, are required to reliably distinguish between less than CT, and reflection-dominated CT models. For instance, the current data are unable to provide informative constraints on Fe Kα line emission (see the Appendix).

4.1.3. SDSS J171350.32+572954.9

For SDSS J1713+5729 there are too few *NuSTAR* counts for broad-band X-ray spectral modeling (see Table 2). Here we investigate the low-energy (<10 keV) spectrum observed with *XMM-Newton*. The object appears to have an extremely steep spectrum at low energies, with PN (MOS) source counts of <2 (<5) at 2–10 keV and 12^{+6}_{-5} (18^{+7}_{-5}) at 0.5–2 keV, implying a photon index of $\Gamma = 3.5^{+1.0}_{-0.8}$ in the 0.5–10 keV energy band; J13 measure a slightly flatter, but consistent (within the uncertainties), value of $\Gamma = 2.5 \pm 0.4$. The steep spectral slope is not typical of an AGN, and would be inconsistent with the *NuSTAR* detection if produced as a result of direct AGN emission. To test whether the soft X-ray emission could be powered by star formation, we compare the 0.5–8 keV luminosity, $L_{0.5-8\,keV} = 1.4 \times 10^{42}$ erg s^{-1}, with the far-infrared (FIR) luminosity, $L_{FIR} < 4.0 \times 10^{44}$ erg s^{-1}, measured using *IRAS* fluxes following Persson & Helou (1987). The relatively high soft X-ray: FIR luminosity ratio of $L_{0.5-8\,keV}/L_{FIR} > 0.0035$, which is a conservative lower limit due to the poorly constrained *IRAS* 100 μm flux, rules out star formation as the driver of the soft X-ray emission (e.g., see Figure 8 of Alexander et al. 2005). We deduce that the soft X-rays detected with *XMM-Newton* are indirectly powered by the AGN (e.g., via photoionization or scattered AGN emission), and *NuSTAR* may have provided the first identification of the directly transmitted (or reflected) AGN continuum of this QSO2.

4.2. X-Ray Spectral Analysis: Band Ratios

X-ray band ratios provide a basic description of the X-ray spectrum, and are useful when there are insufficient counts for detailed spectral modeling. We define the *NuSTAR* band ratio (BR$_{Nu}$) as the ratio of net source counts in the hard band to those in the soft-band, $S_{8-24\,keV}/S_{3-8\,keV}$. Figure 10 shows BR$_{Nu}$ against redshift (z) for the five (of the total nine) *NuSTAR*-observed candidate CTQSO2s which are detected at 8–24 keV, including the three presented in this paper (SDSS J1218+4706, 1243–0232 and 1713+5729) and the two presented in L14 and G14 (SDSS J0011+0056 and 1034 +6001, respectively). The tracks show the expected evolution of BR$_{Nu}$ with z for four different fixed column densities (N_H) computed using a MYTORUS model with an intrinsic photon index of $\Gamma = 1.8$. We compare the measured BR$_{Nu}$ values for the candidate CTQSO2s with these tracks in order to infer N_H. We note that producing the tracks with, instead, a simple ZWABS · POW model results in higher N_H values for the same BR$_{Nu}$. The *NuSTAR*-detected candidate CTQSO2s, in general, have high band ratios compared to AGNs detected in the
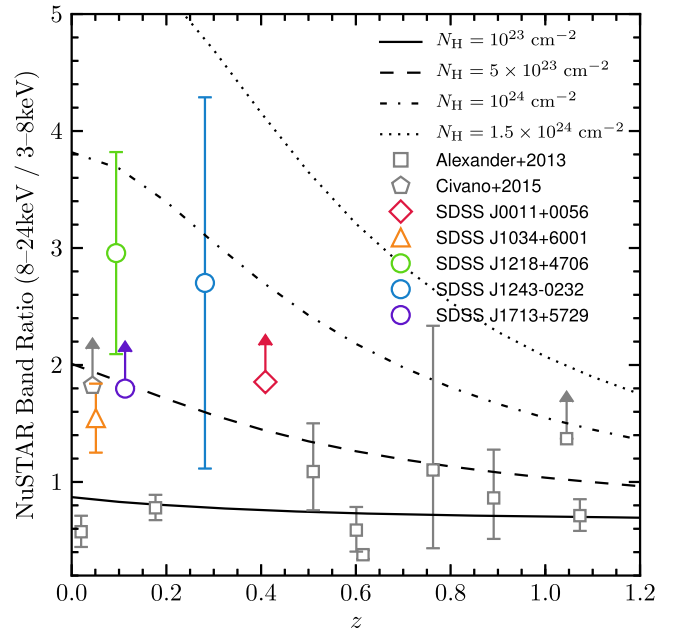

Figure 10. *NuSTAR* band ratio (BR$_{Nu}$) vs. z. The circles, the diamond, and the triangle indicate the candidate CTQSO2s presented in this work, L14 and G14, respectively, which are detected at 8–24 keV; 90% CL error bars and limits are shown. For comparison, gray squares show the first 10 AGNs detected in the *NuSTAR* serendipitous survey (Alexander et al. 2013); 68% CL error bars are shown. The gray pentagon marks a CT AGN identified with *NuSTAR* in the COSMOS field (Civano et al., 2015); a 90% CL lower limit is shown. The tracks show model predictions for BR$_{Nu}$ for four absorbing column densities in the range $N_H = (0.1–1.5) \times 10^{24}$ cm^{-2}. The BR$_{Nu}$ constraints for SDSS J1218 +4706, 1243–0232, and 1713+5729 are higher than that of the confirmed CTQSO2 SDSS J1034+6001 and suggest large absorbing columns.

NuSTAR extragalactic surveys (squares in Figure 10). In all cases the BR$_{Nu}$ values suggest $N_H > 10^{23}$ cm^{-2}.

For SDSS J1713+5729, a *NuSTAR*-detected object with too few counts for broad-band spectral modeling of the direct AGN continuum (see Section 4.1.3), the lower limit in BR$_{Nu}$ suggests heavy absorption with $N_H \gtrsim 5 \times 10^{23}$ cm^{-2}. Our most direct measurement for the intrinsic X-ray luminosity of this QSO2 comes from using this N_H constraint. Taking the observed 10–40 keV luminosity constraint from Table 3, and assuming that the X-ray spectrum is an absorbed power law with $\Gamma = 1.8$, the lower limits obtained are $L^{in}_{2-10\,keV} > 4.6 \times 10^{42}$ erg s^{-1} and $L^{in}_{10-40\,keV} > 5.3 \times 10^{42}$ erg s^{-1}. As an alternative to the BR$_{Nu}$ approach, N_H can be constrained using the *NuSTAR*/*XMM-Newton* band ratio (following L14). However, in this case the constraint ($N_H \gtrsim 2 \times 10^{23}$ cm^{-2}) is less stringent than that from BR$_{Nu}$, due to the comparatively poor quality of the available *XMM-Newton* data.

The N_H estimates made from BR$_{Nu}$ using Figure 10 are relatively crude, since the individual X-ray spectra may have additional spectral complexities (e.g., line emission around ≈ 6.4 keV, a scattered power law, or a complex absorber geometry) not incorporated in our model predictions. To illustrate this, for the two sources with comparatively high quality *NuSTAR* spectra (SDSS J1034+6001 and 1218+4706), the less than CT column densities inferred from the BR$_{Nu}$ analysis ($N_H \lesssim 5 \times 10^{23}$ cm^{-2} and $\lesssim 10^{24}$ cm^{-2}, respectively) are an underestimate of the column densities determined from X-ray spectral fitting ($N_H \gtrsim 1.5 \times 10^{24}$ cm^{-2}; see G14 and Section 4.1.1 of this paper, respectively). Similarly, using the *NuSTAR* results for three CT reflection-dominated Seyfert 2s,
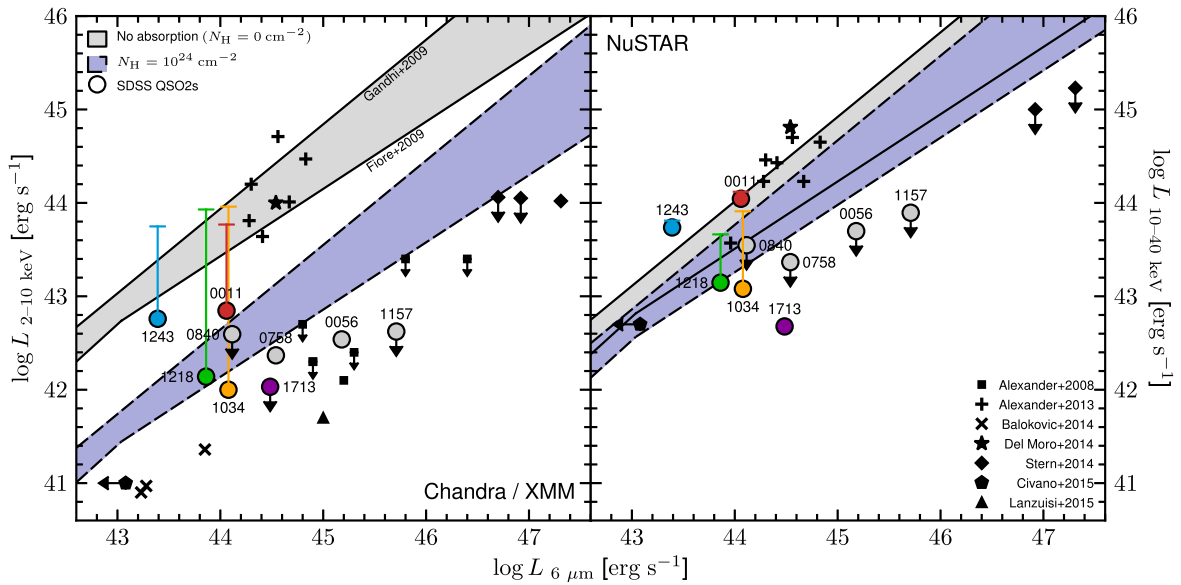
Figure 11. Observed (i.e., uncorrected for absorption) X-ray luminosity for the rest-frame 2–10 keV and 10–40 keV bands (left and right hand panels, respectively) vs. rest-frame 6 μm luminosity (in νL_ν units). The circles indicate the *NuSTAR*-observed SDSS-selected candidate CTQSO2s presented in this work, L14, and G14 ($z = 0.05$–0.49); colored circles mark the *NuSTAR*-detected sources. The X-ray luminosities for the candidate CTQSO2s are taken from best-fitting spectral models where possible. Otherwise, they have been determined from photometry, assuming an unabsorbed power law model with $\Gamma = 0.3$ (as described in Section 3.1). For the three L14 objects (SDSS J0011+0056, 0056+0032 and 1157+6003), the values have been adjusted for consistency with this work. Other *NuSTAR*-observed objects are shown, including: *NuSTAR* extragalactic survey AGNs ("+" symbols; $z = 0.02$–2.92; Alexander et al. 2013), three CT Seyfert 2 AGNs ("×" symbols; $z \approx 0.01$; Baloković et al. 2014), a heavily obscured quasar identified in the ECDFS field (star; $z \approx 2$; Del Moro et al. 2014), three luminous and heavily obscured *WISE*-selected AGNs (diamonds; $z \approx 2$; Stern et al. 2014), and a CT AGN identified in the COSMOS field (pentagon; $z = 0.044$; Civano et al., 2015). For the latter object, we show an upper limit in $L_{6\,\mu m}$, since we have assumed that the mid-IR emission is AGN-dominated. Additionally, for the 2–10 keV band we compare with sources studied at <10 keV with *Chandra* or *XMM-Newton*: the candidate CT quasars presented in Alexander et al. (2008; squares; $z \approx 2$), and a candidate heavily CT AGN identified in the COSMOS field (triangle; $z = 0.35$; Lanzuisi et al. 2015a). For four of the *NuSTAR*-observed candidate CTQSO2s, vertical lines indicate the intrinsic (i.e., corrected for absorption) X-ray luminosities obtained from X-ray spectral analyses. We compare all of the data with two intrinsic relations for the 2–10 keV band (solid black lines): those of Fiore et al. (2009) and Gandhi et al. (2009). Following L14 and Stern et al. (2014), the relations have been extrapolated to 10–40 keV assuming $\Gamma = 1.8$, and the dashed lines show the effect of absorption by $N_H = 10^{24}$ cm^{-2} gas. The different X-ray:mid-IR ratios for the Fiore et al. (2009) and Gandhi et al. (2009) relations means that the former provides a more conservative estimate of the CT absorption threshold. The majority of the *NuSTAR*-observed candidate CTQSO2s have low X-ray:mid-IR ratios, suggesting CT levels of photoelectric absorption.

Baloković et al. (2014) demonstrate that the above BR$_{Nu}$ approach underestimates N_H for reflection-dominated AGNs. Nevertheless, BR$_{Nu}$ provides first-order N_H constraints for weakly detected sources.

4.3. Indirect Constraints on X-Ray Absorption

It is well established that there is a tight relation between the mid-IR and intrinsic X-ray luminosities of AGNs (e.g., Lutz et al. 2004; Fiore et al. 2009; Gandhi et al. 2009; Lanzuisi et al. 2009; Ichikawa et al. 2012; Matsuta et al. 2012; Mateos et al. 2015; Stern 2015). Mid-IR emission can therefore provide an indirect estimate of the intrinsic AGN power, which is especially useful when heavy absorption in the X-rays makes this information challenging to obtain (e.g., Alexander et al. 2008; LaMassa et al. 2009, 2011; Vignali et al. 2010; Goulding et al. 2011; Lanzuisi et al. 2015a). Following the approach used for other *NuSTAR* studies of faint, obscured AGNs (L14; Stern et al. 2014), in Figure 11 we compare the observed X-ray:mid-IR luminosity ratios with intrinsic ratios for unobscured AGNs and those corresponding to X-ray absorption due to dense obscuring material ($N_H = 10^{24}$ cm^{-2}), for both the low- (2–10 keV) and high- (10–40 keV) energy X-ray regimes. We show the full sample of nine *NuSTAR*-observed SDSS-selected candidate CTQSO2s, including the five presented in this work, the three from L14, and the one in G14. The X-ray luminosities (L_X^{obs}) are observed values (i.e., uncorrected for absorption), and the 6 μm luminosities ($L_{6\,\mu m}$,

in νL_ν units) are intrinsic values (i.e., corrected for dust extinction occuring in the system) for the AGN determined through SED modeling (Section 3.3), and both correspond to the values provided in Table 3. We note that for a large fraction of CT AGNs, potentially $\approx 50\%$ in the case of local CT AGNs, we expect significant absorption in the mid-IR (e.g., Bauer et al. 2010; Goulding et al. 2012). We have partially addressed this through dust corrections which are included in the SED modeling (Section 3.3). These corrections are small, however, with the luminosities changing by factors ranging from 1.03 to 1.46 (with a median of 1.17). For the four candidate CTQSO2s with constrained intrinsic X-ray luminosities (L_X^{int}), we plot the L_X^{int} values obtained from X-ray spectral analyses (see L14, G14, and Sections 4.1.1 and 4.1.2 of this work). We conservatively adopt intrinsic X-ray luminosities from the models with lower best-fit column densities (e.g., Model M in the case of SDSS J1218+4706 and the absorbed power law model in the case of SDSS J1243–0232).

The two intrinsic relations utilized for comparison are those of Fiore et al. (2009) and Gandhi et al. (2009), which were both computed at 2–10 keV. In the case of the Gandhi et al. (2009) relation, we adjust the 12 μm (the mid-IR wavelength at which the relation was computed) νL_ν luminosities downward by 7% to obtain 6 μm luminosities based on the Assef et al. (2010) AGN template. The two relations predict slightly different X-ray:mid-IR ratios at low luminosities and diverge further toward higher luminosities, which is partly due to the different

luminosity ranges over which the two relations were calibrated, but also reflects the uncertainty in such relations. Comparison to both allows us to account for systematic effects in the derivation of these relations. We extrapolate the relations to the 10–40 keV band assuming $\Gamma = 1.8$ (typical value for AGNs; e.g., Alexander et al. 2013). An advantage of using 10–40 keV X-ray luminosities ($L_{10-40\,keV}^{obs}$), as opposed to 2–10 keV luminosities ($L_{2-10\,keV}^{obs}$), is that contamination from processes other than AGN continuum emission is negligible in this high-energy band. However, the suppression of the X-ray emission by absorbing gas is less dramatic in the 10–40 keV band, as demonstrated by the relative normalization of the $N_H = 10^{24}$ cm^{-2} lines in the left and right hand panels of Figure 11, which were computed assuming a MYTorus model with $\Gamma = 1.8$ and $\theta_{obs} = 70°$ (following L14). Absorption by $N_H = 10^{24}$ cm^{-2} gas results in a suppression of the X-ray emission by factors of ≈ 20 and ≈ 2 in the 2–10 keV and 10–40 keV bands, respectively. We note that for the four candidate CTQSO2s with L_X^{int} values constrained using X-ray spectral analyses, the intrinsic luminosities agree more closely with the Gandhi et al. (2009) relation than with the Fiore et al. (2009) relation.

In general, the candidate CTQSO2s have extremely low 2–10 keV:mid-IR ratios, with the observed 2–10 keV luminosities a factor of $\gtrsim 20$ lower than the intrinsic relations, suggesting CT absorption. This was already apparent from 2–10 keV luminosities published in the literature, but here we have demonstrated the 2–10 keV suppression using our own soft X-ray analysis. A similar conclusion is reached in the high-energy 10–40 keV band, where six out of nine of the objects have X-ray luminosities a factor of $\gtrsim 2$ lower than the intrinsic relations, consistent with CT obscuration. Our sample of SDSS-selected candidate CTQSO2s lies below the majority of the AGNs detected in the *NuSTAR* extragalactic surveys (Alexander et al. 2013), including a heavily obscured quasar detected in ECDFS (*NuSTAR* J033202–2746.8; $z \approx 2$; Del Moro et al. 2014).

Of the five new objects presented in this work, there is one, SDSS J1243–0232, which does not appear compatible with CT absorption based on this indirect analysis. For this object, the low N_H implied by the relatively high X-ray:mid-IR ratios is incongruous with the direct constraints from X-ray spectral modeling (Section 4.1.2), which suggest $N_H \gtrsim 10^{24}$ cm^{-2}. A similar case where the N_H values inferred from X-ray spectral modeling and the X-ray:mid-IR ratio do not agree is that of *NuSTAR* J033202–2746.8 (the star symbol in Figure 11; Del Moro et al. 2014). Despite the large column density measured for this source ($N_H \approx 6 \times 10^{23}$ cm^{-2}; Del Moro et al. 2014), it lies high with respect to the relations, which may in part be due to its significant Compton reflection component. It is possible that a strong reflection component also contributes to the high X-ray:mid-IR ratio observed for SDSS J1243–0232, especially given that a pure reflection spectrum well describes the data (see Section 4.1.2).

Of the *NuSTAR* targets detected at high energies (>10 keV), SDSS J1713+5729 has the most extreme 10–40 keV:mid-IR ratio, with a $L_{10-40\,keV}^{obs}$ value suppressed by a factor of ≈ 35 with respect to the intrinsic relations (on average). The fact that the source lies even lower than the CTQSO2 SDSS J1034+6001 (G14) may be due to some combination of a heavily CT absorbing column ($N_H \gg 10^{24}$ cm^{-2}) and a less prominent reflection component. For the non-detections, SDSS J0758+3923 and SDSS J0840+3838, the $L_{10-40\,keV}^{obs}$ upper limits

suggest that if the X-ray faintness is due to absorption, these sources are likely CT (for SDSS J0840+3838 this only applies for the Gandhi et al. 2009 relation). While heavy absorption seems the most likely explanation for the X-ray faintness of these non-detections, we do not have broad-band X-ray spectral constraints and therefore cannot rule out the possibility of intrinsic X-ray weakness (e.g., Gallagher et al. 2001; Wu et al. 2011; Luo et al. 2014; Teng et al. 2014). However, intrinsic X-ray weakness is a phenomenon observed for type 1 sources where there is an unobscured view of the central nucleus, unlike for our QSO2s.

5. DISCUSSION

In the following sections, we discuss the possible implications of the extremely high column densities and corresponding intrinsic luminosities measured for the *NuSTAR*-detected heavily obscured QSO2s presented in this paper (SDSS J1218+4706, 1243–0232 and 1713+5729), L14 (SDSS J0011+0056), and G14 (SDSS J1034+6001) in the context of the overall quasar population.

5.1. Heavy Absorption and Powerful X-Ray Luminosities

Figure 12 shows N_H versus intrinsic (i.e., absorption-corrected) X-ray luminosity for all SDSS-selected QSO2s that have been studied at low energies (<10 keV) with *Chandra* and *XMM-Newton*, and have *direct* constraints from X-ray spectral analyses. The intrinsic X-ray luminosities shown are for the rest-frame 2–10 keV band ($L_{2-10\,keV}^{in}$) and are hereafter referred to as L_X. The data are compiled from J13 and LaMassa et al. (2014). Since these two studies have different approaches, with the former limiting the spectral analysis to absorbed power law models and the latter using physically motivated models, we adopt the LaMassa et al. (2014) values where multiple measurements exist. Overlaid are the five sources which have 8–24 keV detections with *NuSTAR*, for which it is therefore possible to remeasure N_H and L_X with the addition of the high-energy (>10 keV) data. In each case, there is a range of column densities consistent with the data. To be conservative, we adopt measured values at the lower end of these ranges: e.g., for SDSS J1218+4706 we adopt the `Model M` results ($N_H = 2.0 \times 10^{24}$ cm^{-2}; Section 4.1.1) and for SDSS J1243–0232 we adopt the absorbed power law model results ($N_H = 9 \times 10^{23}$ cm^{-2}; Section 4.1.2). The improvements made with *NuSTAR* are illustrated by the colored lines, which connect the literature constraints prior to *NuSTAR* and the broad-band, *NuSTAR* plus soft X-ray constraints.

Our L_X and N_H constraints for these five objects are significantly higher than the constraints in the literature from spectral modeling of the soft X-ray (*Chandra* or *XMM-Newton*) data alone. For the fainter quasars which have net *Chandra* (0.5–8 keV) or *XMM-Newton* PN (0.5–10 keV) source counts of $S_{soft} \lesssim 15$ (SDSS J0011+0056, 1243–0232, and 1713+5729) the soft X-ray constraints underpredict N_H by factors of $k_{N_H} \approx 30$–1600, while for the brighter sources with $S_{soft} \gtrsim 50$ (SDSS J1034+6001 and 1218+4706) N_H is underpredicted by factors of $k_{N_H} \approx 2.5$–5. In general, the intrinsic X-ray luminosities (L_X) measured are ≈ 1–2 orders of magnitude higher with the addition of *NuSTAR* data, which is largely due to the increased absorption correction. These results have implications for X-ray studies of AGNs at $z < 1$ that lack sensitive high-energy (>10 keV) coverage. For example, on the
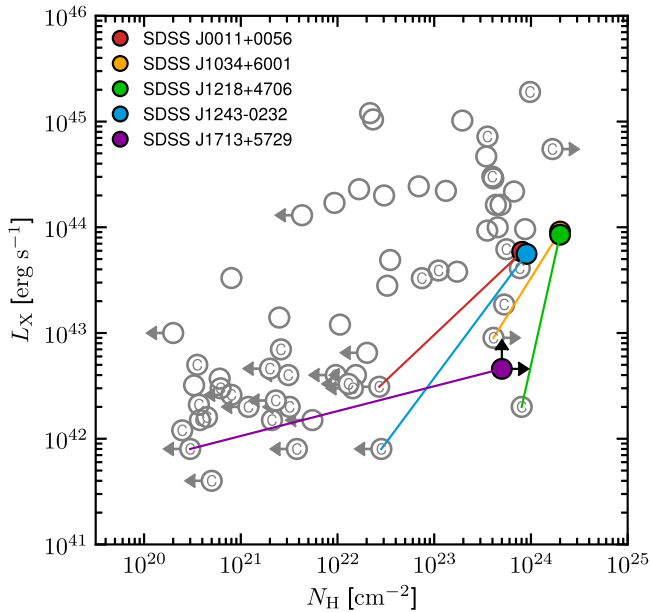
Figure 12. Intrinsic (i.e., absorption-corrected) rest-frame 2–10 keV luminosity ($L_{2-10\,\mathrm{keV}}^{\mathrm{in}}$, or L_X) vs. N_H for SDSS-selected QSO2s, as measured from X-ray spectral analyses. The gray open circles show the constraints in the literature, all directly measured from X-ray spectral fitting at soft X-ray energies (<10 keV; J13; LaMassa et al. 2014). Sources with evidence for being CT, primarily based on the indirect X-ray:[O III] luminosity ratio diagnostic, are marked with a "C". The colored circles show our constraints for the five NuSTAR-observed candidate CTQSO2s detected at high energies (>10 keV) from the broad-band NuSTAR plus soft X-ray spectral analyses presented in this study, L14, and G14. The colored lines indicate the significant increase in both L_X and N_H for these five objects between the soft X-ray constraints in the literature and the NuSTAR plus soft X-ray studies. We note that for SDSS J1243–0232 the increase in L_X shown (blue line) may be an overestimate.[33]

Figure 13. N_H distribution of SDSS-selected QSO2s at $z < 0.5$, constructed using only direct constraints from X-ray spectral analyses. The five NuSTAR-observed objects with enough >10 keV counts for X-ray spectral analyses are marked by the hatched regions. Left panel: a measurement of the N_H distribution from existing soft X-ray (<10 keV) Chandra and XMM-Newton constraints. CT candidates, identified as such in J13 and LaMassa et al. (2014) primarily using the indirect X-ray:[O III] luminosity ratio diagnostic, are labeled as "CT." Sources with upper/lower limits in N_H are marked with arrows. Right panel: prediction for the true N_H distribution of SDSS-QSO2s based on the results of this broad-band NuSTAR plus soft X-ray study; see Section 5.2.

basis of our results we infer that X-ray data at <10 keV may not reliably identify heavily obscured to CT ($N_H \gtrsim 5 \times 10^{23}$ cm^{-2}) AGNs if the photon counts are low, and the intrinsic luminosities will be underestimated. A similar conclusion was reached by Wilkes et al. (2013), who used Chandra and multiwavelength data to investigate the intrinsic X-ray properties of quasars selected at low radio frequencies.

The intrinsic X-ray luminosities of our objects (close to $L_X = 10^{44}$ erg s^{-1}, which roughly agrees with the $L_{X,*}$ value for unobscured AGNs; e.g., Hasinger et al. 2005) makes them important for population synthesis models of the CXB since $z \lesssim 1.5$ AGNs around this luminosity produce most of the CXB at its high-energy peak (e.g., Treister & Urry 2005).[32] It is thus useful to consider the N_H distribution and CT fraction for this class of optically selected QSO2s.

5.2. The N_H Distribution

In the left panel of Figure 13 we show the observed N_H distribution for SDSS-selected QSO2s that are detected with Chandra and XMM-Newton, and have *direct* constraints at <10 keV from X-ray spectral fitting (J13; LaMassa et al. 2014). The 39 objects included have $z < 0.5$ and $L_{[\mathrm{O\,III}]} > 2.5 \times 10^8\,L_{\odot}$,

and should therefore be broadly representative of the overall optically selected QSO2 population (for further details, see Section 2.2). The exclusion of QSO2s undetected by Chandra and XMM-Newton has a negligible impact since, for the adopted z and $L_{[\mathrm{O\,III}]}$ ranges, there are only three such objects. On the basis of these data, the column density distribution is relatively flat at $N_H = 10^{21} - 10^{24}$ cm^{-2}, and there is only one object above $N_H = 10^{24}$ cm^{-2}. The absorber for this object (SDSS J0939+3553) appears different in nature to those presented in this paper, possibly taking the rare form of a geometrically thin toroidal ring (LaMassa et al. 2014).

In this work, we have demonstrated that soft X-ray (Chandra and XMM-Newton) studies can underpredict the N_H and L_X values of quasars with evidence for CT absorption based on multiwavelength diagnostics (CT candidates; see Section 5.1 and Figure 12). The severity of the N_H and L_X underpredictions is related to the observed soft X-ray source photon counts (S_{soft}), with the faintly detected sources suffering larger underpredictions than the more strongly detected sources. To understand the consequences of this for the true N_H distribution of QSO2s, our result for the NuSTAR-detected objects can be extrapolated to the remaining CT candidates in Figure 13, which were identified as such primarily based on the X-ray:[O III] luminosity ratio (J13; LaMassa et al. 2014). This extrapolation relies on assuming that the NuSTAR-detected subsample of five objects are representative of the remaining subsample of 19 CT candidates in terms of their absorption properties. This is a reasonable assumption; the $L_X^{\mathrm{obs}}/L_{6\,\mu\mathrm{m}}$ distributions of the two subsamples are in agreement (KS test: $p = 0.70$) using the X-ray luminosities from J13 (except for SDSS J1243–0232, for which we use our measured luminosity; see footnote 33) and estimating the 6 μm luminosities from an interpolation between the WISE photometric bands.

To make a prediction for the true N_H distribution of optically selected QSO2s, we apply an N_H correction factor (k_{N_H}) to each of the 19 CT candidates in Figure 13 not observed/detected

---

[32] While the NuSTAR-detected objects all satisfy the classical optical quasar luminosity definition (see Sections 2.1 and 2.2), based on Figure 12 they are just below the standard "X-ray quasar" luminosity threshold ($L_X > 10^{44}$ erg s^{-1}), although SDSS J1034+6001, 1218+4706, and 1243–0232 are consistent with lying above the threshold for some of the X-ray spectral model solutions.
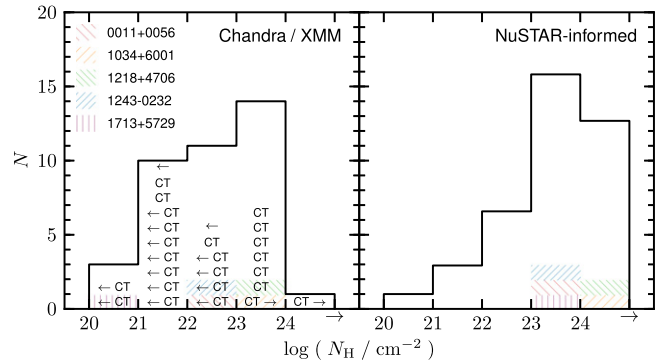
[33] For SDSS J1243–0232, we measure a significantly higher Chandra flux (by roughly a factor of eight) than J13 using the same data. While there is not a clear reason for this discrepancy, we note that our measured Chandra 3–8 keV flux agrees well with the NuSTAR flux for the same energy band (see Table 3).

with *NuSTAR*, informed by our *NuSTAR*-measured k_{N_H} values (Section 5.1). For sources with low ($S_{soft} < 33$) and high ($S_{soft} > 33$) soft X-ray source counts (using PN counts only in the case of *XMM-Newton* data) we draw correction factors at random from flat distributions between $1.5 < \log(k_{N_H}) < 3.2$ and between $0.4 < \log(k_{N_H}) < 0.7$, respectively. In determining these correction factors we assumed column densities that are at the lower end of the range that is consistent with the data (Section 5.1): for the three most strongly detected sources (SDSS J1034+6001, 1218+4706, 1243–0232), the lowest best-fit N_H values of $(0.9–2.0) \times 10^{24}$ cm^{-2} are adopted, although the sources are consistent with having much larger columns ($N_H \gtrsim 5 \times 10^{24}$ cm^{-2}) and we assume the N_H lower limit for SDSS J1713+5729 ($N_H = 5 \times 10^{23}$ cm^{-2}). As such, the N_H distribution prediction below may provide a lower limit on the CT fraction. However, this discussion is ultimately limited by the small number of sources detected above 10 keV with *NuSTAR*.

The predicted N_H distribution (averaged over many iterations) is shown in the right-hand panel of Figure 13. This "*NuSTAR*-informed" N_H distribution for optically selected QSO2s is strongly skewed toward high columns of $N_H > 10^{23}$ cm^{-2}. Our predicted CT fraction (f_{CT}), defined here as the ratio of the number of objects with $N_H > 10^{24}$ cm^{-2} to those with $N_H > 10^{22}$ cm^{-2}, is $f_{CT} = 36^{+14}_{-12}\%$, where the errors represent binomial uncertainties only. The full uncertainties are likely to be larger; considering extreme k_{N_H} distributions, where the k_{N_H} values assumed are all set equal to either the highest or lowest values of the ranges measured with *NuSTAR*, the uncertainties on f_{CT} may be larger by a factor of ≈ 2.

The CT fraction is an important parameter in population synthesis models of the CXB. In many such models, f_{CT} is treated as a fixed, global quantity; the Treister et al. (2009) model assumes a relatively low value of 15%, while others assume 50% (Gilli et al. 2007; Ueda et al. 2014; the quoted fractions have been adjusted from the original published values to our adopted definition of f_{CT}). It is possible to estimate f_{CT} using this class of CXB synthesis models, although meaningful constraints are challenging to obtain due to degeneracies with other parameters (e.g., Akylas et al. 2012). Fixing the Compton reflection strength parameter, Ueda et al. (2014) constrain $f_{CT} = 33\%–62\%$, which is compatible with our result. In other CXB synthesis models, the CT fraction is dependent on physical properties of the AGN population; according to the Draper & Ballantyne (2010) model, high CT fractions are associated (beyond the local universe) specifically with black holes accreting at a large fraction of their Eddington rate, in broad consistency with our findings.

With the N_H distribution in Figure 13 we have attempted to provide a prediction using only *directly* measured column densities since analysis of the X-ray spectrum should provide the "purest" measurement of the line of sight column density, without the need to make assumptions in comparing emission across very different wavelength regimes (i.e., using *indirect* absorption diagnostics such as the X-ray:mid-IR, X-ray:[O III] or X-ray:[Ne V] luminosity ratios). However, it is worthwhile considering an extreme scenario in which all of the candidate CTQSO2s in Figure 13 (labeled "CT") are truly CT; i.e., in which the indirect absorption diagnostics are assumed to be accurate. Applying this assumption, the predicted CT fraction is $f_{CT} = 65^{+11}_{-13}\%$. For comparison, Vignali et al. (2010) make

similar assumptions using the X-ray:[O III] and X-ray:mid-IR luminosity ratios for a complete sample of 25 SDSS-selected QSO2s at $z \approx 0.5$, and determine $f_{CT} \approx 50\%$. Additionally, Vignali et al. (2014) utilize the X-ray:[Ne V] ratio for a sample of $z \approx 0.8$ type 2 AGNs and find $f_{CT} \approx 40\%$. In the case of Seyfert 2s in the local universe, N_H distributions have been constructed for optically selected samples using indirect absorption diagnostics (primarily the X-ray:[O III] ratio), predicting a fraction of $f_{CT} \gtrsim 50\%$ for this lower luminosity AGN population (e.g., Bassani et al. 1999; Risaliti et al. 1999; LaMassa et al. 2011).

Indirect absorption diagnostics predict a larger CT fraction for $z < 0.5$ QSO2s than our *NuSTAR*-informed N_H distribution. The apparent discrepancy may well be due to indirect diagnostics overpredicting the number of CT AGNs. Another reconciling factor could be that the quasars unobserved/undetected with *NuSTAR*, in general, suffer even heavier absorption than our detected objects. Deeper observations at both low (e.g., with *Athena*; Nandra et al. 2013) and high (e.g., with *NuSTAR* or *Astro-H*; Takahashi et al. 2012) X-ray energies are needed to reliably distinguish between the above scenarios and thus achieve tighter constraints on f_{CT} for the quasar population.

6. SUMMARY

Sensitive high-energy (>10 keV) *NuSTAR* observations of five optically selected candidate CTQSO2s have been presented along with broad-band X-ray spectral and multi-wavelength analyses. Similar studies for a further four such objects have already been presented in the literature (L14; G14). The overall sample of nine $z < 0.5$ candidate CTQSO2s was selected primarily on the basis of multi-wavelength evidence for absorption by CT ($N_H > 1.5 \times 10^{24}$ cm^{-2}) material along the line of sight (see Section 2.2). Our results are summarized as follows.

1. Of the five recently observed objects, two are undetected by *NuSTAR* at 8–24 keV (SDSS J0758+3923 and 0840+3838), one is weakly detected (net source counts $S_{8-24\,keV} = 38.1^{+19.6}_{-18.1}$; SDSS J1713+5729), and two are strongly detected ($S_{8-24\,keV} \gtrsim 90$; SDSS J1218+4706 and 1243–0232). These represent the first detections of these sources at high X-ray energies; see Section 3.1.

2. For the two strongly detected targets, spectral modeling of the *NuSTAR* plus archival soft X-ray data suggests that the primary transmitted AGN continua are suppressed by extreme levels of photoelectric absorption, with $N_H \gtrsim 10^{24}$ cm^{-2}; see Section 4.1. For the brightest source, SDSS J1218+4706, the relatively high quality spectral analysis using physically motivated models provides strong evidence for CT absorption, with a contribution from Compton reflection; see Section 4.1.1.

3. For SDSS J1713+5729, the *NuSTAR* detection likely represents the first identification of directly transmitted emission from the AGN; see Section 4.1.3. We characterize the 3–24 keV spectrum using the *NuSTAR* band ratio (BR$_{Nu}$) and estimate a high absorbing column density of $N_H \gtrsim 5 \times 10^{23}$ cm^{-2}; see Section 4.2. Notably, the observed 10–40 keV luminosity appears to be extremely suppressed, by a factor of ≈ 35, with respect to the intrinsic luminosity, suggesting $N_H \gg 10^{24}$ cm^{-2} if purely due to absorption; see Section 4.3.

4. For the non-detections, column densities of $N_{\mathrm{H}} \gtrsim 10^{24}$ cm^{-2} are inferred by comparing the upper limits in observed X-ray luminosity (at rest-frame 2–10 keV and 10–40 keV) with the intrinsic luminosities expected from the mid-IR emission. The majority of *NuSTAR*-observed candidate CTQSO2s have X-ray:mid-IR ratios suggesting CT absorption; see Section 4.3.

5. For the five objects in the overall *NuSTAR*-observed candidate CTQSO2 sample that are detected at high energies, the column densities and intrinsic luminosities measured from spectral analyses are factors of ≈ 2.5–1600 and ≈ 10–70 higher, respectively, than soft X-ray constraints in the literature; see Section 5.1.

6. Using direct constraints on absorption for 39 QSO2s studied at X-ray wavelengths, and assuming that the *NuSTAR*-detected QSO2s are representative of the larger sample with evidence for CT absorption, we make a prediction for the N_{H} distribution of optically selected QSO2s. The distribution is highly skewed toward large column densities ($N_{\mathrm{H}} > 10^{23}$ cm^{-2}) and the predicted CT fraction of $f_{\mathrm{CT}} = 36^{+14}_{-12}\%$ is broadly consistent with CXB models. A higher fraction of up to 76% is possible if indirect absorption diagnostics are assumed to be accurate; see Section 5.2.

APPENDIX

Here we give further information on the individual *NuSTAR*-observed candidate CTQSO2s presented in this paper, namely relevant multiwavelength properties and features which provide evidence for CT material (Section A.1). In the case of X-ray properties, this Section focuses on the low-energy (<10 keV) *Chandra* and *XMM-Newton* data which were available prior to the *NuSTAR* observations. For the broad-band X-ray constraints incorporating high-energy (>10 keV) *NuSTAR* data, which generally suggest extreme absorption, see Section 4. In addition, we discuss the identification of a strong Fe Kα line in the *XMM-Newton* spectrum of SDSS J0011+0056, the single *NuSTAR* detection in the exploratory candidate CTQSO2 sample presented by L14 (Section A.2). Lastly, we provide the near-UV to mid-IR photometric data used in the SED modeling (Section A.3).

A.1 Additional Information for Individual Objects

A.1.1 SDSS J075820.98+392336.0 (z = 0.216)

Fitting an unabsorbed power law model to the *XMM-Newton* 0.5–10 keV data, we measure a flat effective photon index of $\Gamma_{\mathrm{eff}} = 1.1 \pm 0.4$, indicative of photoelectric absorption in the X-ray spectrum. This source is not detected (above the 2.6σ CL) with *NuSTAR* at 8–24 keV; see Section 3.1.

A.1.2 SDSS J084041.08+383819.8 (z = 0.313)

From *Hubble Space Telescope* (*HST*) WFPC2 (F814W) imaging (Villar-Martín et al. 2012), the host has a spiral morphology with evidence for a tidal feature. Humphrey et al. (2010) included this object in their integral-field observations of six SDSS-QSO2s and found spatially extended [O III] and [O II] emission on scales of up to 27 kpc, consistent with being powered by AGN activity (e.g., via shocks or radiation). Using the available *XMM-Newton* 0.5–10 keV data for this object we measure $\Gamma_{\mathrm{eff}} = 0.7 \pm 0.1$, a low value suggestive of heavy absorption. This source is a non-detection in the *NuSTAR* 8–24 keV data; see Section 3.1.

A.1.3 SDSS J121839.40+470627.7 (z = 0.094)

The 0.5–10 keV *XMM-Newton* (obsID 0203270201) spectrum is modeled in J13 and LaMassa et al. (2012), who measure high column densities of $N_{\mathrm{H}} = 8.0^{+5.6}_{-4.1} \times 10^{23}$ cm^{-2} and $N_{\mathrm{H}} = (8.7^{+6.7}_{-3.4}) \times 10^{23}$ cm^{-2}, respectively. J13 measure a strong Fe Kα feature at $E_{\mathrm{line}} = 6.4 \pm 0.2$ keV with $\mathrm{EW}_{\mathrm{Fe\,K}\alpha} = 1.7^{+2.4}_{-1.4}$ keV, consistent with CT absorption. This target is strongly detected with *NuSTAR* at 8–24 keV, allowing relatively detailed, broad-band spectral modeling which extends to high energies (>10 keV); see Section 4.1.1.

A.1.4 SDSS J124337.34−023200.2 (z = 0.281)

Using *HST* Advanced Camera for Surveys imaging, Zakamska et al. (2006) find that the host galaxy light profile is well fit by a de Vaucouleurs profile, implying an elliptical morphology. The host morphology is notably asymmetric. Zakamska et al. (2006) find no evidence for extinction in the host galaxy, suggesting that kiloparsec-scale dust is not obscuring the AGN, and measure a blue excess in the nucleus which may be due to scattering or starburst emission.

Table 5
Near-ultraviolet to Mid-infrared Source Properties

SDSS J	0758+3923	0840+3838	1034+6001	1218+4706	1243−0232	1713+5729
u (0.355 μm)[a]	18.967 ± 0.025	20.349 ± 0.179	16.139 ± 0.008	18.727 ± 0.030	20.604 ± 0.116	18.721 ± 0.025
g (0.468 μm)[a]	18.423 ± 0.008	19.166 ± 0.023	14.743 ± 0.002	17.562 ± 0.008	19.334 ± 0.018	17.480 ± 0.006
r (0.616 μm)[a]	17.792 ± 0.007	18.021 ± 0.014	14.342 ± 0.002	16.843 ± 0.008	18.015 ± 0.010	16.629 ± 0.004
i (0.748 μm)[a]	17.629 ± 0.008	17.627 ± 0.013	13.871 ± 0.002	16.386 ± 0.008	17.782 ± 0.012	16.133 ± 0.004
z (0.892 μm)[a]	17.706 ± 0.019	17.171 ± 0.026	13.698 ± 0.004	16.180 ± 0.014	17.391 ± 0.029	16.093 ± 0.009
WISE (3.4 μm)[b]	13.847 ± 0.028	14.322 ± 0.029	11.187 ± 0.024	12.592 ± 0.023	14.762 ± 0.040	12.466 ± 0.023
WISE (4.6 μm)[b]	12.267 ± 0.024	13.549 ± 0.035	10.016 ± 0.021	11.448 ± 0.021	14.348 ± 0.063	11.060 ± 0.021
WISE (12 μm)[b]	8.659 ± 0.022	10.013 ± 0.041	6.295 ± 0.014	8.242 ± 0.019	11.270 ± 0.155	7.242 ± 0.015
Spitzer (3.6 μm)[c]	...	...	...	...	279.100 ± 3.333	...
Spitzer (4.5 μm)[c]	...	...	...	...	258.600 ± 3.668	...
Spitzer (5.8 μm)[c]	...	...	...	...	280.000 ± 10.640	...
Spitzer (8.0 μm)[c]	...	...	...	...	535.300 ± 14.130	...

Notes.
[a] SDSS DR7 model magnitudes in the AB sinh system, corrected for Galactic extinction.
[b] WISE magnitudes in the Vega system. We use the gmag magnitude for SDSS J1713+5729, and profile-fit magnitudes for the remainder.
[c] Spitzer 3″8 diameter aperture flux densities in units of μJy.

Studying the existing *Chandra* data, we find an excess of emission at observed-frame $\approx$5 keV (i.e., rest-frame $\approx$6.4 keV). When fitting the continuum emission with a power law and the excess with a Gaussian component, we measure a rest-frame centroid energy compatible with Fe Kα ($E_{\rm line} = 6.5^{+0.7}_{-0.2}$ keV), and a rest-frame equivalent width of $EW_{\rm Fe\ K\alpha} = 2.5^{+4.2}_{-2.4}$ keV. Although the emission is consistent with $EW_{\rm Fe\ K\alpha} \gtrsim 1$ keV, which would suggest the presence of CT material, there are too few photon counts to rule out low equivalent widths. The object appears to have an extremely flat spectrum, with $\Gamma_{\rm eff} = -1.1^{+1.2}_{-1.6}$ for the 0.5–8 keV energy band, indicating strong photoelectric absorption. This target is strongly detected at 8–24 keV with *NuSTAR*, allowing broad-band X-ray spectral modeling; see Section 4.1.2.

A.1.5 SDSS J171350.32+572954.9 (z = 0.113)

The mid-IR spectrum, as measured with *Spitzer*-IRS (Sargsyan et al. 2011), is AGN-dominated and has evidence for shallow silicate (Si) absorption at $\approx$10 μm. The low-energy X-ray properties of this source are detailed in Section 4.1.3. To summarize, an extremely steep spectral shape at 0.5–10 keV ($\Gamma \approx 3$) suggests that the weak *NuSTAR* detection at 8–24 keV is the first identification of directly transmitted AGN emission from this system.

A.2 An Iron Line in the X-Ray Spectrum of SDSS J001111.97+005626.3

The $<$10 keV X-ray spectrum of SDSS J0011+0056 was first presented in J13. L14 extended the X-ray analysis to high energies and used the *NuSTAR/XMM-Newton* band ratio to identify heavy, close to CT, absorption ($N_{\rm H} \approx 8 \times 10^{23}$ cm^{-2}). L14 did not perform detailed spectral modeling, due to the low source counts ($\approx$25 net source counts). However, studying the *XMM-Newton* 0.5–10 keV spectrum we find evidence for an excess at observed frame $\approx$4.5 keV (i.e., rest-frame $\approx$6.4 keV). Modeling the continuum emission with a power law and the excess with a Gaussian component, the rest-frame line centroid energy is in good agreement with that expected for Fe Kα line emission ($E_{\rm line} = 6.4 \pm 0.1$ keV) and the rest-frame equivalent width is large ($EW_{\rm Fe\ K\alpha} = 2.9^{+2.5}_{-2.2}$ keV). This strong Fe Kα

emission suggests CT absorption, and it adds confidence to the high column density measured by L14.

A.3 Near-ultraviolet to Mid-infrared Photometry

In Table 5 we provide the near-UV to mid-IR photometric data set for the five *NuSTAR*-observed QSO2s presented in this work and the one presented in G14 (SDSS J1034+6001). This data set is adopted for the SED modeling in Section 3.3.

REFERENCES

Akylas, A., Georgakakis, A., Georgantopoulos, I., Brightman, M., & Nandra, K. 2012, A&A, 546, A98
Alexander, D. M., Bauer, F. E., Chapman, S. C., et al. 2005, ApJ, 632, 736
Alexander, D. M., Chary, R.-R., Pope, A., et al. 2008, ApJ, 687, 835
Alexander, D. M., Stern, D., Del Moro, A., et al. 2013, ApJ, 773, 125
Antonucci, R. 1993, ARA&A, 31, 473
Arnaud, K. A. 1996, in ASP Conf. Ser. 101, Astronomical Data Analysis Software and Systems V, ed. G. H. Jacoby & J. Barnes (San Francisco, CA: ASP), 17
Assef, R. J., Eisenhardt, P. R. M., Stern, D., et al. 2015, ApJ, 804, 27
Assef, R. J., Kochanek, C. S., Brodwin, M., et al. 2008, ApJ, 676, 286
Assef, R. J., Kochanek, C. S., Brodwin, M., et al. 2010, ApJ, 713, 970
Assef, R. J., Stern, D., Kochanek, C. S., et al. 2013, ApJ, 772, 26
Baloković, M., Comastri, A., Harrison, F. A., et al. 2014, ApJ, 794, 111
Bassani, L., Dadina, M., Maiolino, R., et al. 1999, ApJS, 121, 473
Bauer, F. E., Arevalo, P., Walton, D. J., et al. 2014, ApJ, submitted (arXiv:1411.0670)
Bauer, F. E., Yan, L., Sajina, A., & Alexander, D. M. 2010, ApJ, 710, 212
Baumgartner, W. H., Tueller, J., Markwardt, C. B., et al. 2013, ApJS, 207, 19
Brightman, M., & Nandra, K. 2011, MNRAS, 413, 1206
Buchner, J., Georgakakis, A., Nandra, K., et al. 2015, ApJ, 802, 89
Burlon, D., Ajello, M., Greiner, J., et al. 2011, ApJ, 728, 58
Cash, W. 1979, ApJ, 228, 939
Civano, F., Hickox, R., Puccetti, S., et al. 2015, ApJ, in press
Comastri, A. 2004, in Astrophysics and Space Science Library 308, Supermassive Black Holes in the Distant Universe, ed. A. J. Barger (Dordrecht: Kluwer), 245
Comastri, A., Ranalli, P., Iwasawa, K., et al. 2011, A&A, 526, L9
Comastri, A., Setti, G., Zamorani, G., & Hasinger, G. 1995, A&A, 296, 1
Del Moro, A., Mullaney, J. R., Alexander, D. M., et al. 2014, ApJ, 786, 16
Donoso, E., Yan, L., Stern, D., & Assef, R. J. 2014, ApJ, 789, 44
Draper, A. R., & Ballantyne, D. R. 2010, ApJL, 715, L99
Fabian, A. C. 1999, MNRAS, 308, L39
Fabian, A. C., Vasudevan, R. V., Mushotzky, R. F., Winter, L. M., & Reynolds, C. S. 2009, MNRAS, 394, L89
Fiore, F., Puccetti, S., Brusa, M., et al. 2009, ApJ, 693, 447
Gallagher, S. C., Brandt, W. N., Laor, A., et al. 2001, ApJ, 546, 795
Gandhi, P., Horst, H., Smette, A., et al. 2009, A&A, 502, 457

Gandhi, P., Lansbury, G. B., Alexander, D. M., et al. 2014, ApJ, 792, 117
Gandhi, P., Yamada, S., Ricci, C., et al. 2015, MNRAS, 449, 1845
George, I. M., & Fabian, A. C. 1991, MNRAS, 249, 352
Ghisellini, G., Haardt, F., & Matt, G. 1994, MNRAS, 267, 743
Gilli, R., Comastri, A., & Hasinger, G. 2007, A&A, 463, 79
Gilli, R., Su, J., Norman, C., et al. 2011, ApJL, 730, L28
Goulding, A. D., Alexander, D. M., Bauer, F. E., et al. 2012, ApJ, 755, 5
Goulding, A. D., Alexander, D. M., Mullaney, J. R., et al. 2011, MNRAS,
    411, 1231
Hainline, K. N., Hickox, R., Greene, J. E., Myers, A. D., & Zakamska, N. L.
    2013, ApJ, 774, 145
Harrison, F. A., Craig, W. W., Christensen, F. E., et al. 2013, ApJ, 770, 103
Hasinger, G., Miyaji, T., & Schmidt, M. 2005, A&A, 441, 417
Hazard, C., Mackey, M. B., & Shimmins, A. J. 1963, Natur, 197, 1037
Heckman, T. M., Ptak, A., Hornschemeier, A., & Kauffmann, G. 2005, ApJ,
    634, 161
Hickox, R. C., Jones, C., Forman, W. R., et al. 2007, ApJ, 671, 1365
Hopkins, P. F., Hernquist, L., & Cox, T. J. 2008, Kereš, D ApJS, 175, 356
Humphrey, A., Villar-Martín, M., Sánchez, S. F., et al. 2010, MNRAS, 408, L1
Ichikawa, K., Ueda, Y., Terashima, Y., et al. 2012, ApJ, 754, 45
Iwasawa, K., Gilli, R., Vignali, C., et al. 2012, A&A, 546, A84
Jia, J., Ptak, A., Heckman, T., & Zakamska, N. L. 2013, ApJ, 777, 27
Kalberla, P. M. W., Burton, W. B., Hartmann, D., et al. 2005, A&A, 440, 775
Koss, M., Mushotzky, R., Baumgartner, W., et al. 2013, ApJL, 765, L26
Kraft, R. P., Burrows, D. N., & Nousek, J. A. 1991, ApJ, 374, 344
Lacy, M., Ridgway, S. E., Sajina, A., et al. 2015, ApJ, 802, 102
LaMassa, S. M., Heckman, T. M., & Ptak, A. 2012, ApJ, 758, 82
LaMassa, S. M., Heckman, T. M., Ptak, A., et al. 2009, ApJ, 705, 568
LaMassa, S. M., Heckman, T. M., Ptak, A., et al. 2010, ApJ, 720, 786
LaMassa, S. M., Heckman, T. M., Ptak, A., et al. 2011, ApJ, 729, 52
LaMassa, S. M., Yaqoob, T., Ptak, A. F., et al. 2014, ApJ, 787, 61
Lansbury, G. B., Alexander, D. M., del Moro, A., et al. 2014, ApJ, 785, 17
Lanzuisi, G., Perna, M., Delvecchio, I., et al. 2015a, A&A, in press
    (arXiv:1505.01153)
Lanzuisi, G., Piconcelli, E., Fiore, F., et al. 2009, A&A, 498, 67
Lanzuisi, G., Ranalli, P., Georgantopoulos, I., et al. 2015b, A&A, 573, A137
Lonsdale Persson, C. J., & Helou, G. 1987, ApJ, 314, 513
Luo, B., Brandt, W. N., Alexander, D. M., et al. 2013, ApJ, 772, 153
Luo, B., Brandt, W. N., Alexander, D. M., et al. 2014, ApJ, 794, 70
Lutz, D., Maiolino, R., Spoon, H. W. W., & Moorwood, A. F. M. 2004, A&A,
    418, 465
Madsen, K. K., Harrison, F. A., Markwardt, C., et al. 2015, arXiv:1504.01672
Magdziarz, P., & Zdziarski, A. A. 1995, MNRAS, 273, 837
Maiolino, R., Salvati, M., Bassani, L., et al. 1998, A&A, 338, 781
Mateos, S., Alonso-Herrero, A., Carrera, F. J., et al. 2013, MNRAS, 434, 941
Mateos, S., Carrera, F. J., Alonso-Herrero, A., et al. 2015, MNRAS, 449, 1422

Mateos, S., Carrera, F. J., Page, M. J., et al. 2010, A&A, 510, A35
Matsuta, K., Gandhi, P., Dotani, T., et al. 2012, ApJ, 753, 104
Murphy, K. D., & Yaqoob, T. 2009, MNRAS, 397, 1549
Nandra, K., Barret, D., Barcons, X., et al. 2013, arXiv:1306.2307
Nousek, J. A., & Shue, D. R. 1989, ApJ, 342, 1207
Ptak, A., Zakamska, N. L., Strauss, M. A., et al. 2006, ApJ, 637, 147
Reyes, R., Zakamska, N. L., Strauss, M. A., et al. 2008, AJ, 136, 2373
Risaliti, G. 2002, A&A, 386, 379
Risaliti, G., Maiolino, R., & Salvati, M. 1999, ApJ, 522, 157
Sanders, D. B., Soifer, B. T., Elias, J. H., et al. 1988, ApJ, 325, 74
Sargsyan, L., Weedman, D., Lebouteiller, V., et al. 2011, ApJ, 730, 19
Schmidt, M. 1963, Natur, 197, 1040
Schmidt, M., & Green, R. F. 1983, ApJ, 269, 352
Scott, A. E., Stewart, G. C., Mateos, S., et al. 2011, MNRAS, 417, 992
Simpson, C. 2005, MNRAS, 360, 565
Smith, R. K., Brickhouse, N. S., Liedahl, D. A., & Raymond, J. C. 2001, ApJL,
    556, L91
Stern, D. 2015, ApJ, 807, 129
Stern, D., Assef, R. J., Benford, D. J., et al. 2012, ApJ, 753, 30
Stern, D., Lansbury, G. B., Assef, R. J., et al. 2014, ApJ, 794, 102
Takahashi, T., Mitsuda, K., Kelley, R., et al. 2012, Proc. SPIE, 8443, 1
Teng, S. H., Brandt, W. N., Harrison, F. A., et al. 2014, ApJ, 785, 19
Treister, E., & Urry, C. M. 2005, ApJ, 630, 115
Treister, E., Urry, C. M., Schawinski, K., Cardamone, C. N., & Sanders, D. B.
    2010, ApJL, 722, L238
Treister, E., Urry, C. M., & Virani, S. 2009, ApJ, 696, 110
Ueda, Y., Akiyama, M., Hasinger, G., Miyaji, T., & Watson, M. G. 2014, ApJ,
    786, 104
Ueda, Y., Akiyama, M., Ohta, K., & Miyaji, T. 2003, ApJ, 598, 886
Urry, C. M., & Padovani, P. 1995, PASP, 107, 803
Vignali, C., Alexander, D. M., & Comastri, A. 2006, MNRAS, 373, 321
Vignali, C., Alexander, D. M., Gilli, R., & Pozzi, F. 2010, MNRAS, 404, 48
Vignali, C., Mignoli, M., Gilli, R., et al. 2014, A&A, 571, A34
Villar-Martín, M., Cabrera Lavers, A., Bessiere, P., et al. 2012, MNRAS,
    423, 80
Wachter, K., Leach, R., & Kellogg, E. 1979, ApJ, 230, 274
Weisskopf, M. C., Wu, K., Trimble, V., et al. 2007, ApJ, 657, 1026
Werner, M. W., Roellig, T. L., Low, F. J., et al. 2004, ApJS, 154, 1
Wik, D. R., Hornstrup, A., Molendi, S., et al. 2014, ApJ, 792, 48
Wilkes, B. J., Kuraszkiewicz, J., Haas, M., et al. 2013, ApJ, 773, 15
Wright, E. L., Eisenhardt, P. R. M., Mainzer, A. K., et al. 2010, AJ, 140, 1868
Wu, J., Brandt, W. N., Hall, P. B., et al. 2011, ApJ, 736, 28
Yaqoob, T. 1997, ApJ, 479, 184
York, D. G., Adelman, J., Anderson, J. E., Jr., et al. 2000, AJ, 120, 1579
Zakamska, N. L., Strauss, M. A., Krolik, J. H., et al. 2003, AJ, 126, 2125
Zakamska, N. L., Strauss, M. A., Krolik, J. H., et al. 2006, AJ, 132, 1496